PAPER

Check for updates

Enhanced electrocatalytic hydrogen evolution *via* nitrogen-induced electron density modulation in ReSe2/2D carbon heterostructures†

Zakhele B. Ndala, [ID] *[abc] Ndivhuwo P. Shumbula,[d] Seiso E. Tsoeu,[a] Thelma W. Majola,[a] Siziwe S. Gqoba,[a] Cebisa E. Linganiso,[abc] Zikhona N. Tetana[e] and Nosipho Moloto [ID] *[a]

The synthesis of heterostructures composed of transition metal dichalcogenides (TMDs) and carbon nanostructures has garnered a lot of attention in recent years. This is due to the synergistic effects that arise from these heterostructures that are advantageous in various applications. This includes but is not limited to the improvement in electron conductivity of TMDs that are grown on carbon nanostructures. This improvement in electron conductivity can increase the catalytic activity of TMDs towards the hydrogen evolution reaction (HER). Therefore, it is crucial to understand the formation of these heterostructures and how the interaction of the component materials can improve their performance as electrocatalysts in the HER. This study highlights how surface chemistry affects heterostructure formation and the catalytic performance of heterostructures in the HER. ReSe2 nanocrystals were grown on 2D carbon nanostructures, specifically reduced graphene oxide (rGO), nitrogen doped reduced graphene oxide (N-rGO), and graphitic carbon nitride (g-C3N4). FTIR, XPS, and TEM analyses showed that functional groups on carbon surfaces play a key role in the formation of the heterostructures. Among the materials tested, rGO had the highest ReSe2 loading due to the availability of oxygen containing functional groups on the surface of rGO. However, the performance of the heterostructures as catalysts in the HER showed that ReSe2-N-rGO had the highest catalytic activity with the lowest onset potential (115 mV), Tafel slope (72 mV dec^{-1}), and overpotential (218 mV). The enhanced performance of the ReSe2-N-rGO catalyst was due to the modulation of rGO by nitrogen doping which improved the electron transfer between ReSe2 and N-rGO, this was further confirmed using computational studies and by ReSe2-N-rGO having the lowest R_{ct} (65 Ω).

1. Introduction

Layered materials such as transition metal dichalcogenides (TMDs) have enjoyed increasing popularity in recent years due to their exploration in various applications such as in energy storage and generation devices, sensors, and biological

[a]Molecular Science Institute, School of Chemistry, University of the Witwatersrand, Private Bag 3, Wits 2050, South Africa. E-mail: zakhele.ndala@wits.ac.za; Nosipho. Moloto@wits.ac.za; Tel: +2711 717 1339

[b]DST/NRF Centre of Excellence in Strong Materials, University of the Witwatersrand, Private Bag 3, Wits 2050, South Africa

[c]Microscopy and Microanalysis Unit, University of the Witwatersrand, Private Bag 3, Wits 2050, Johannesburg, South Africa

[d]Health Platform, Advanced Materials Division, Mintek, 200 Malibongwe Drive, Randburg, South Africa

[e]Institute for Nanotechnology and Water Sustainability, College of Science, Engineering and Technology, University of South Africa, Florida Campus, Johannesburg 1709, South Africa

† Electronic supplementary information (ESI) available. See DOI: https://doi.org/10.1039/d5ra01096a

applications.[1-4] The interest regarding these materials arises from the interesting properties they exhibit when in their monolayer or few layer forms. These properties include relatively high carrier mobility, chemical reactivity, high surface area, and the transition from indirect to direct bandgaps in some cases.[5-7] These properties have been modified in certain cases to increase performance in given applications. The interlayer spacing of these materials has been expanded to better accommodate cations for battery applications[8] and the morphology of the materials has also been altered to increase the exposure of the active edge sites of these materials for electrocatalytic production of hydrogen.[9] Moreover, these materials have been used as one of many components in heterostructures to improve some of their inherent properties. TMDs have been combined with carbon nanostructures to make TMD/carbon heterostructures with improved performance in the hydrogen evolution reaction (HER).[10] These heterostructures have shown improved catalytic activity towards the HER, this has been thought to be due to improved electron transfer processes due to the enhanced electron conductivity

provided by the carbon nanostructures.[11–13] This has led to further exploration on the formation of heterostructures between TMDs and various carbon nanostructures. Consequently, there has also been concerted effort to form these heterostructures with nitrogen doped carbon nanostructures because they offer higher electron conductivity compared to their undoped counterparts.[14–16] The formation of TMD/N-doped carbon nanostructures could significantly increase the catalytic activity of the heterostructures towards the HER through the increased conductivity of the N-doped carbon nanostructures.[16] Graphitic carbon nitride has been shown to be an excellent photocatalyst for the production of hydrogen and has been used a support materials for various metal nanoparticles to relative success.[17,18] Although g-C$_3$N$_4$ is not considered an exceptional catalyst for HER due to poor conductivity and electrochemical activity, there have been attempts to increase its effectiveness in the HER through forming heterostructures with certain nanostructures.[19] The incorporation of TMDs on different carbon nanostructure variations could open up new avenues for increasing catalytic activity towards the HER. This work focuses on the synthesis of ReSe$_2$/2D carbon nanostructure heterostructures and their catalytic activity towards the HER. ReSe$_2$ has already been shown to be a promising electrocatalyst for the HER.[20,21] The 2D carbon nanostructures selected were reduced graphene oxide (rGO), nitrogen doped reduced graphene oxide (N-rGO), graphitic carbon nitride (g-C$_3$N$_4$). ReSe$_2$ nanocrystals were grown on the surface of the surface of the 2D carbon nanostructures and the catalytic activity of the formed heterostructures towards the HER was evaluated.

2. Experimental section

2.1 Chemicals

Ammonium perrhenate (NH$_4$ReO$_4$, 99.98%), selenium powder (Se, 99.99%), oleic acid (90%), reduced graphene oxide (90%), and melamine (99%). All reagents were purchased from Sigma-Aldrich and used as received without purification.

2.2 Synthesis of nanostructures

2.2.1 Reduced graphene oxide. The reduced graphene oxide was purchased from Sigma-Aldrich.

2.2.2 Doping of rGO. A quartz tube was purged with Ar for 60 min while the temperature was increased to 800 °C at a rate of 10 °C min^{-1}. The rGO was doped using ammonia gas as the nitrogen source, with Ar as the carrier gas at a flow-rate of 50 ml min^{-1}. The temperature was held at 800 °C for 3 h then cooled to room temperature.

2.2.3 Synthesis of g-C$_3$N$_4$. Melamine (5 g) was placed in a quartz boat and heated in a quartz tube to 600 °C for 2 h with an initial heating rate of 20 °C min^{-1}. After that, the deammonization was performed at 600 °C for another 2 h. The yellow product obtained was sonicated in isopropanol for 1 h.

2.2.4 Synthesis of ReSe$_2$-rGO, ReSe$_2$-N-rGO, and ReSe$_2$-gC$_3$N$_4$ heterostructures. The selenium powder (Se, 0.559 mmol) was added into a three-neck round bottom flask containing 20 ml of oleic acid at room temperature. The temperature was increased to 220 °C to thermally reduce the Se to Se^{2-} with the help of the solvent, which also acted as a reducing agent. A sample vial containing 30 mg of rGO/N-rGO/g-C$_3$N$_4$, ammonium perrhenate (NH$_4$ReO$_4$, 0.186 mmol), and 5 ml of oleic acid was sonicated for 30 minutes. The vial was then heated to dissolve the ammonium perrhenate and injected into the Se–oleic acid mixture at 220 °C. The temperature was then raised to 330 °C and the reaction was run for 120 min. The nanoparticles formed were then washed with ethanol and toluene using a centrifuge and then left to dry.

2.3 Characterization techniques

The phase purity, crystallinity, and preferred crystal orientation of the products were examined using powder X-ray diffraction (PXRD) on a Bruker MeasSrv D2-205530 diffractometer using secondary graphite monochromated CuKα radiation (λ 1.5406 Å) at 30 kV/10 mA. Measurements were taken using a glancing angle of incidence detector at an angle of 2°, for 2θ values over 10–70° in steps of 0.026° with a step time of 37 s and at a temperature of 25 °C. The Raman spectroscopy was conducted using the Horiba MacroRam spectrophotometer with a 785 nm wavelength at 5% laser power. The XPS measurements of the powder samples were obtained using a Thermo ESCAlab 250Xi with Al Kα photon source (1486.7 eV), X-ray power of 300 W, X-ray spot size of 900 μm, pass energy (survey) of 100 eV, pass energy (20 eV), and pressure of <10^{-8} mbar. The sample morphologies were determined using transmission electron microscopy (TEM) carried out on an FEI Tecnai T12 TEM microscope operated at an acceleration voltage of 120 kV. The TEM samples were prepared by sonicating a spatula tip of the sample in ethanol and drop-casting that dispersion on a lacey carbon Cu grid. The total surface area and pore volume of the nanostructures were ascertained using a Micromeritics TriStar 3000 Surface Area and Porosity Analyzer. Thermal analysis was done using a PerkinElmer TGA 6000 thermogravimetric analyzer using high purity nitrogen and air at a heating rate of 10 °C min^{-1} and gas flow rate of 20 ml min^{-1}. The morphology of the synthesized materials were characterized by using scanning electron microscopy (SEM) measurements (LEO, Zeiss SEM).

2.4 Electrochemical characterization

The electrochemical measurements were carried out on a BASi epsilon E2. All measurements were carried out in 0.5 M H$_2$SO$_4$ using a three-electrode system. An Ag/AgCl electrode was used as the reference electrode, a platinum wire was used as the counter electrode. A modified glassy carbon electrode with a 3 mm diameter was used as the working electrode. The ink or fresh dispersion of the sample was prepared by dispersing 5.0 mg of the ReSe$_2$ or the ReSe$_2$ and rGO/N-rGO/g-C$_3$N$_4$ heterostructures with 0.5 mg carbon black and 40 μl of Nafion solution (5 wt%) in a 1 ml mixture of water and isopropanol at a 3 : 1 ratio. The solution was then sonicated for 30 min and ~5 μl of the ink was drop-casted onto the glassy carbon electrode. The electrode was allowed to dry at room temperature. The

linear sweep voltammograms were obtained at a scan rate of 2 mV s^{-1} and the cyclic voltammograms were obtained at a potential range of 0.2–0.6 V *vs.* RHE at 100 mV s^{-1} scan rate. The measured potentials *vs.* Ag/AgCl were converted to the reversible hydrogen electrode (RHE) scale according to the Nernst equation:

$$E_{RHE} = E_{Ag/AgCl} + 00059 \text{ pH} + E^0_{Ag/AgCl} \qquad (1)$$

where E_{RHE} is the converted potential *vs.* RHE, $E^0_{Ag/AgCl} = 0.210$ V at 25 °C. The impedance spectroscopy studies were conducted on a Biologic SP 300, the measurements were done at a potential of −200 mV *vs.* RHE and a frequency range between 0.1 Hz and 100 kHz.

2.5 Computational analysis

The parameter calculations in this study were conducted using CASTEP in the BIOVIA Material Studio package of the density functional theory (DFT) method.[22] Geometrical optimization calculations were performed at $2 \times 2 \times 1$ *k*-points, with non-polarized effects consideration. The exchange correlation between electrons was treated with the Perdew–Burke–Ernzerhof (PBE) function within the generalized gradient approximation (GGA).[23,24] Considering the convergence criteria for structural geometric optimization, the energy of tolerance of 2.0 10^{-6} eV per atom was adopted, together with 600 eV plane wave energy cut off. The vacuum layer thickness is fixed at 15 Å to avoid interlayer interactions. The *k*-points used to optimise the ReSe$_2$ sheet were heterostructure $a = 6.651$ Å, $b = 6.750$ Å and $c = 43.012$ Å. To avoid the lattice constraints mismatch of GO-graphiticN/ReSe$_2$ heterostructure and GO-pyridinicN/ReSe$_2$ heterostructure $a = 6.814$ Å, $b = 6.863$ Å and $c = 12.468$ Å and $a = 6.597$ Å, $b = 6.765$ Å and $c = 11.574$ Å were used for both 2D heterostructures respectively. To describe the stability of the formed 2D heterostructures, the binding energies are defined as:[25]

$$E_b = (E_{GO/ReSe_2} - E_{GO} - E_{ReSe_2})/S \qquad (2)$$

$$E_b = (E_{GO\text{-graphiticN}/ReSe_2} - E_{GO\text{-graphiticN}} - E_{ReSe_2})/S \qquad (3)$$

where E_b, E_{GO}, $E_{GO\text{-graphiticN}}$, E_{ReSe_2}, $E_{GO\text{-graphiticN}/ReSe_2}$ and represents the total binding energies of GO sheet, GO-graphiticN, ReSe$_2$ structure, and GO-graphiticN/ReSe$_2$ heterostructure, respectively. S represents the interface area in the plane.[26]

3. Results and discussion

Powder X-ray diffraction (PXRD) was used to characterize the phase, composition, and crystallinity of the nanostructures. The PXRD patterns of reduced graphene oxide (rGO) and nitrogen-doped reduced graphene oxide (N-rGO) are shown in Fig. 1(a).

The (002) peak is observed for both the rGO and N-rGO at 26.6° and 26.8° respectively (JCPDS card no: 75-2078). This peak is indicates a high degree of graphitization, which alludes to the formation of a well-arranged layer structure.[27] The appearance

of the (100), (004), and (110) peaks at 43.8°, 54.7°, and 77.8° degrees respectively indicates that the rGO nanosheets are not monolayer.[27,28] There is an observable shift to the right in the (002) peak in the N-rGO sample as shown in Fig. 1(b), this has been attributed to the doping of nitrogen in the graphene oxide lattice structure.[28] Sherrer's equation can be used to determine crystallite size along the (002) plane which can be used as an estimate for the thickness of the rGO nanosheets, the thickness was determines to be 16.34 nm for rGO and 14.4 nm for N-rGO. The thickness is reduced in N-rGO because of the removal of oxygen containing functional groups during the doping process. The PXRD pattern of g-C$_3$N$_4$ is shown in Fig. 1(c), the characteristic diffraction peaks of g-C$_3$N$_4$ were observed (JCPDS: 87-1526).[29] The main peak at $2\theta = 27.8°$ corresponds to the (002) plane, which is ascribed to the distance between the layers of the graphitic material with an interlayer spacing of 0.323 nm. The peak at $2\theta = 13.7°$ corresponds to the (001) diffraction plane, this peak is attributed to the intra-layer *d*-spacing (0.651 nm). The g-C$_3$N$_4$ synthesized through poly-condensation is typically considered to have low crystallinity, as is the case in this study. This is due to the incomplete deamination of the precursors which results in the formation of a tri-*s*-triazine-based melon structure which consists of in-plane infinite one-dimensional chains of NH-bridged melem oligomers. The diffractogram for the graphitic carbon nitride synthesized in this study is similar to that of bulk g-C$_3$N$_4$ also signifying the formation of the tri-*s*-triazine melon structure.[29] The powder patterns of the ReSe$_2$ and carbon heterostructures is shown in Fig. 1(d). The diffraction peaks as shown in Fig. 1(d) are observed at 13.7°, 31.9°, 35.2°, 42.6°, 47.1°, and 55.2°. These diffraction peaks correspond to the lattice planes (001), (1−22), (−220), (012), (003) and (1−42) of ReSe$_2$. The broad diffraction peak between $2\theta = 30–40°$ is attributed to the overlap of smaller peaks in that region, this has been observed in nanosized ReSe$_2$ materials.[21] The PXRD confirms that the ReSe$_2$ nanostructures have crystallized in the distorted 1T phase triclinic system with the $P\bar{1}$ space group (JCPDS card no: 01-065-4275). The (002) peak of the rGO, N-rGO, and g-C$_3$N$_4$ can still be observed in the powder patterns of the heterostructures which alludes to the incorporation of the ReSe$_2$ nanostructures on the 2D carbon nanostructures. Raman spectroscopy was also used to characterize the rGO and N-rGO. This was done by analyzing the characteristic D, G, and 2D bands of the nanostructures. The Raman spectra of the rGO and N-rGO are shown in Fig. 1(e). The position of the G-band in rGO and N-rGO was observed at ~1588 cm^{-1} and 1591 cm^{-1} respectively, this is in accordance with what has been previously reported in the literature.[30] The G-band is attributed to the in-plane stretching vibrations of the sp^2 hybridized carbon–carbon bonds. The D band is associated with the defects that exist in the structure of the materials. The D-bands of the rGO and N-rGO were observed at 1316 cm^{-1} and 1307 cm^{-1} respectively. The broad and high-intensity D band observed in both the undoped rGO and N doped rGO signifies a high level of lattice distortion and sp^3 like defects which show that there are functional groups on the surface of the rGO and N-rGO.[27] The rGO was further reduced in the doping process which occurred at 800 °C. The I_D/I_G ratio of the N-rGO was found
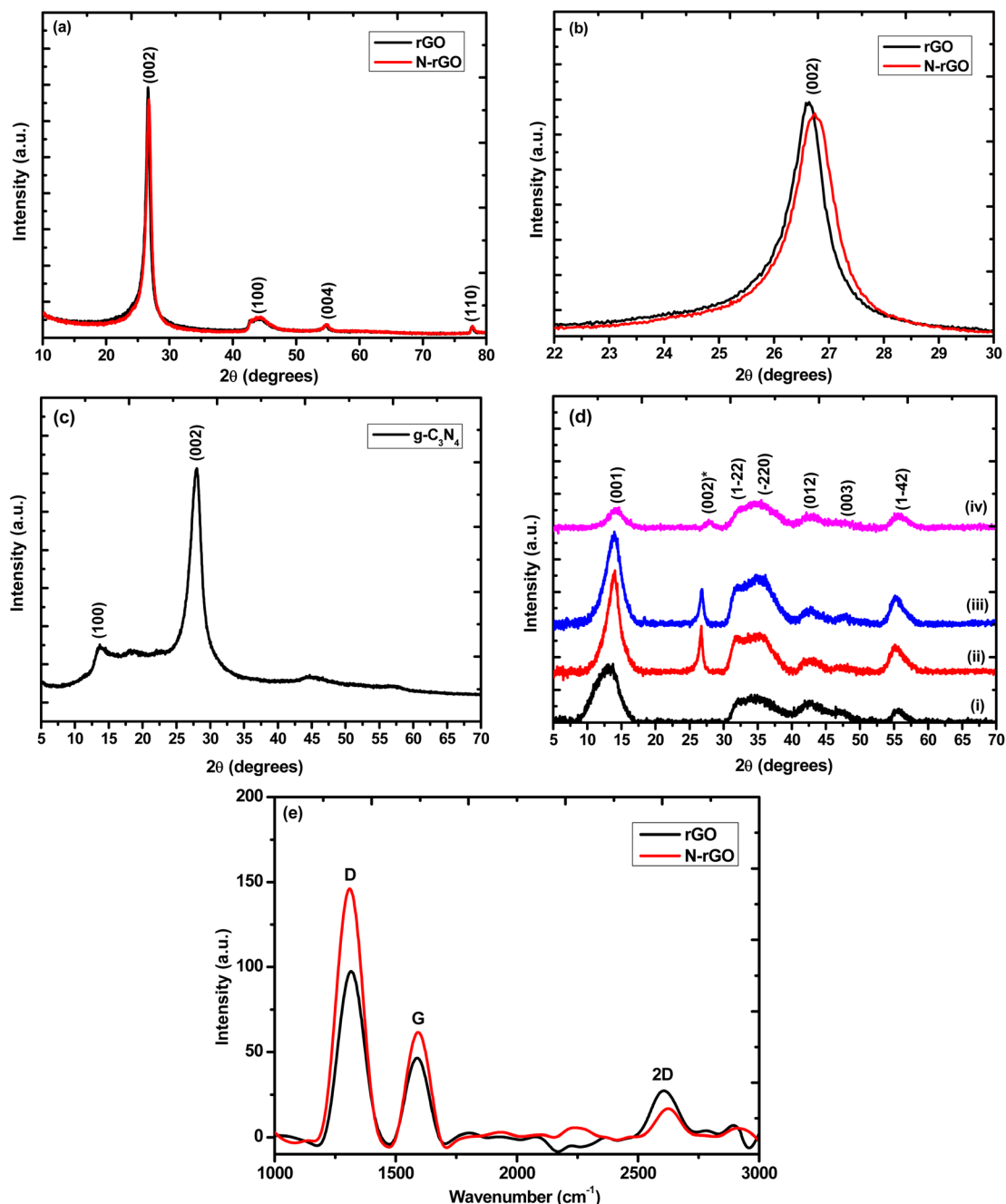
Fig. 1 PXRD patterns of (a) rGO and N–rGO. (b) PXRD shows the shift of the (002) in rGO and N–rGO. (c) The PXRD pattern of g-C$_3$N$_4$ (d) PXRD pattern of (i) pristine ReSe$_2$, (ii) ReSe$_2$-rGO, (iii) ReSe$_2$-N–rGO, and (iv) ReSe$_2$-g-C$_3$N$_4$. (e) Raman spectra of rGO and N–rGO.

to be 2.09 which was higher than that of the rGO at 1.86, this indicates that there is an increase in the number of defects in the structure of the N-rGO which is due to the nitrogen-doping.[31] The 2D peak occurs due to two lattice vibrational processes, this peak can be used to assess the quality of graphene because it is very sensitive to disorder. It is normally very prominent in highly crystalline high-quality graphene. The peak experiences a decrease in intensity when there are defects in the structure of the materials.[30] The notable decrease in the intensity of the 2D peak of the N-rGO compared to the rGO is

indicative of the introduction of more disorder in the structure through the introduction of nitrogen defects.

X-ray photoelectron spectroscopy (XPS) was used to evaluate the bonding configuration and the elemental composition of the nanostructures. The XPS spectra of rGO and N-rGO are shown in Fig. S1(a) and (b).† The C1s and O1s peaks were detected in the survey scan of the rGO nanostructures. The survey scan of the N-rGO nanomaterials also shows the N1s peak which confirms the doping of the rGO with nitrogen.[32] The elemental composition of rGO and N-rGO is shown in Table 1.

Table 1 Summary of the elemental composition of rGO and N-rGO

Sample	Element	Binding energy (eV)	Atomic (%)
rGO	C	284.9	86.4
	O	532.8	13.6
	N	—	—
N-rGO	C	284.4	97.5
	O	532.7	1.6
	N	399.1	0.9

The elemental composition shows that the percentage of oxygen is much larger in rGO compared to the N-rGO. This shows that the rGO contains more of oxygen-containing functional groups and that some of these functional groups are removed in the doping process. The elemental composition of the N-rGO only shows a nitrogen doping concentration of 0.9%. The C1s spectra of the rGO and N-rGO are shown in Fig. S2(a) and (b)† and a summary of the atomic composition is shown in Table 2.

The peak binding energies were found to be 284.9 eV, 285.8 eV, and 288.7 for C–C, C–O, and O–C=O functional groups respectively for rGO.[33] The peak binding energies were found to be 284.4 eV and 285.7 for C–C and C–O functional groups respectively for N-rGO.[33] Table 2 shows there is a notable decrease in the amount of oxygen-containing functional groups in N-rGO, this is due to the removal of the functional groups during doping. The N1s spectrum of N-rGO is shown in Fig. 2(a), the N1s peak can be deconvoluted into several individual peaks, namely the pyridinic-N (398.1–399.3 eV), pyrrolic-N (399.8–401.2 eV), and graphitic-N (401.1–402.7 eV).[33,34] These characteristic peaks are observed in the N1s XPS spectrum and are shown in Fig. 2(a), the nitrogen-doped graphene oxide seems to be dominated by pyridinic-N sites followed by pyrrolic-N sites. The graphitic-N sites are the least prevalent, while the peak at 405 eV is attributed to chemisorbed nitrogen oxide. The types of nitrogen defects introduced are shown graphically in Fig. 2(b). The XPS survey spectra of g-C$_3$N$_4$ is shown in Fig. S1(c).† The high-resolution N1s and C1s spectra are shown in Fig. 2(c) and (d) respectively. The N1s spectrum shows the 3 characteristic peaks of g-C$_3$N$_4$.[35] The main peak at 398.0 eV is due to sp^2 hybridized nitrogen in the triazine ring (C–C=N) (N1), the peak

at 399.8 eV was ascribed to the tertiary nitrogen in the heptazine unit (N2), the peak at 401.4 eV was ascribed to the amino groups carrying hydrogen (N3), the peak at 403.8 eV was ascribed to the NO$_x$ species (N4).[35] The C1s spectra shows the three characteristic peaks. The peak at 284.4 eV has been shown to be due to the C–C (C1) bonds in graphitic carbon while the peak at 288.4 eV was ascribed to the sp^2 bonded carbon (N–C=N) of the triazine and heptazine rings (C2).[35] The peak at 285.8 can be attributed to a nitrile species –C=N (C3). The peak at 288.5 eV is due to the C–O bonding which suggest that there exist some oxygen groups on the surface of the graphene sheets (C4), this is confirmed in the XPS survey spectrum as shown in Fig. S1(c).† The XPS survey spectra of pristine ReSe$_2$ is shown in Fig. S1(d).† The XPS spectra of the Re4f and Se3d are shown in Fig. 2(e) and (f) respectively.

The high-resolution XPS spectrum of Re^{4+} is shown in Fig. 2(e), the core level peaks 4f$_{7/2}$ and 4f$_{5/2}$ were measured at 41.2 eV and 43.6 eV respectively.[21] The Se high-resolution XPS spectrum of the ReSe$_2$ nanomaterials is shown in Fig. 2(f). The deconvoluted peak at ∼54 eV shows the characteristic core level 3d$_{5/2}$ and 3d$_{3/2}$ peaks Se^{2-} at 53.7 eV and 54.7 eV respectively.[21] The XPS survey spectra of the heterostructures is shown in Fig. S3(a)–(c),† the high-resolution spectra of the Re^{4+} and Se^{2-} is also shown in Fig. S4(a)–(f).† The XPS spectra of the analysis of the O1s spectra was used to investigate possible interactions between the ReSe$_2$ and the carbon nanostructures. Table 3 shows a summary of the binding energy of the O1s spectra of the rGO, N-rGO, and the heterostructures, the O1s spectra is shown in Fig. S5(a)–(d).†

Table 3 shows that the binding energy of the O1s spectrum of ReSe$_2$-rGO shifted by ∼0.3 eV from the pristine rGO. The same phenomenon was observed for the ReSe$_2$-N-rGO, a noticeable shift in the binding of the assigned peaks. This indicates that the chemical environment rGO functional group had been altered due to the growth of the ReSe$_2$ nanostructures on the surface of the rGO and N-rGO. Table S1† shows a summary of the binding energy of Re4f$_{7/2}$. A shift in the binding energy of 0.3 eV and 0.5 eV in the Re4f$_{7/2}$ for ReSe$_2$-rGO and ReSe$_2$-N-rGO further indicates an interaction between the oxygen functional groups in rGO and N-rGO. The Re^{4+} XPS spectra are shown in Fig. S4(b) and (d).† The high-resolution N1s and C1s spectrum of ReSe$_2$-g-C$_3$N$_4$ are shown in Fig. S4(g) and (h).† The characteristic peaks of carbon nitride are observed in the N1s and C1s spectra of the heterostructure. However, there is an approximately 0.5 eV shift in the characteristic N1s peaks of the ReSe$_2$-g-C$_3$N$_4$ compared to the g-C$_3$N$_4$. This shows a change in the chemical environment of the nitrogen groups in the carbon nitride structure. This indicates that there is a chemical interaction between the nitrogen groups in the carbon nitride cavities and the ReSe$_2$ nanostructures. The C1s spectrum of the heterostructures shows a slight shift and repression of the C2 peak which confirms that the ReSe$_2$ nanostructures interact with the nitrogen groups in the heptazine and triazine structure of the carbon nitride. This was further explored using FTIR. The FTIR spectra of the g-C$_3$N$_4$ and ReSe$_2$-g-C$_3$N$_4$ are shown in Fig. S6.† The typical characteristic peaks of g-C$_3$N$_4$ observed at 1318 cm^{-1}, 1393 cm^{-1}, 1534 cm^{-1}, and 1621 cm^{-1} were

Table 2 Summary of the C1s assignments and composition

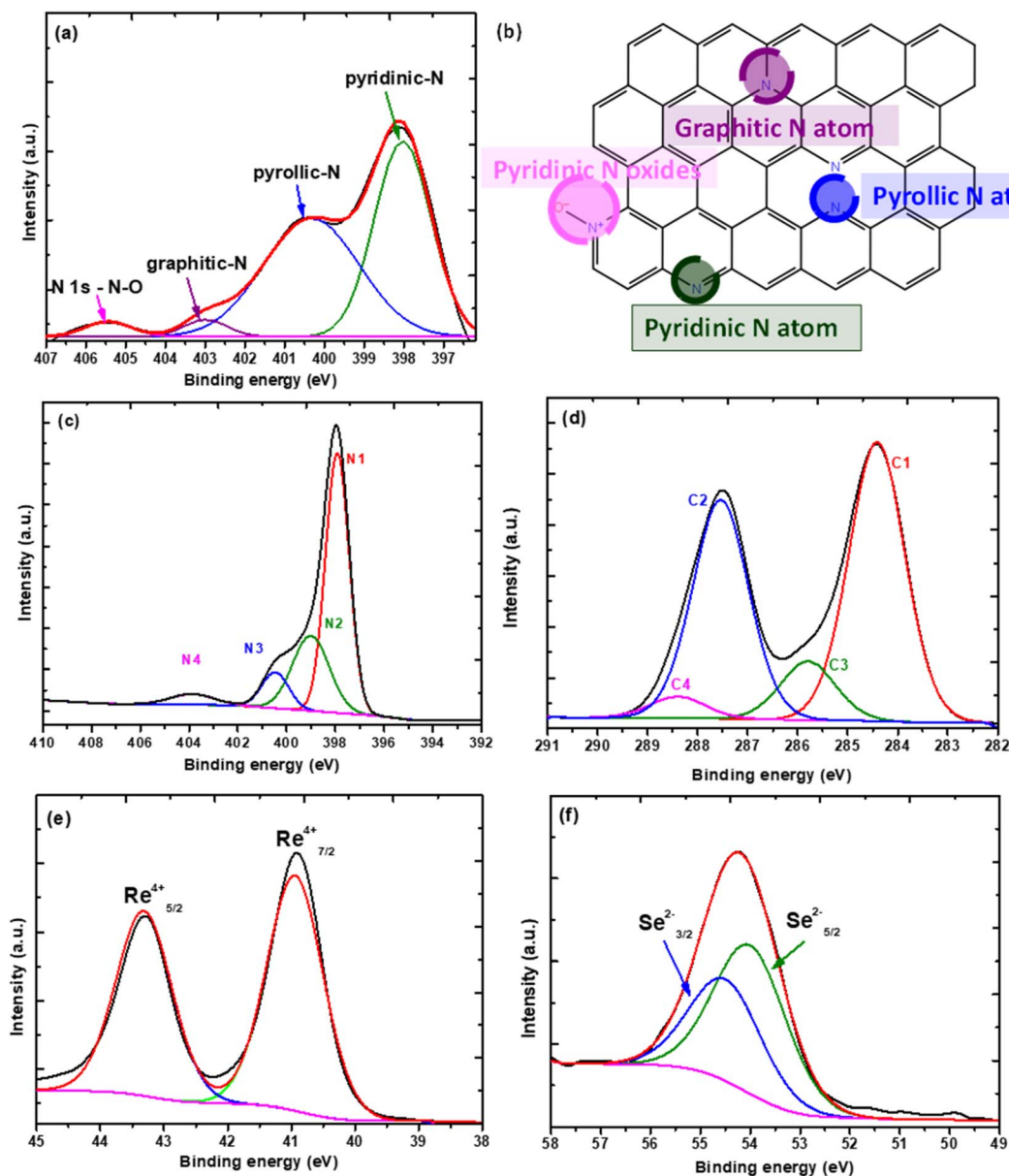| Sample	Assignment	Binding energy (eV)	Atomic (%)
rGO	C–C sp^2	284.2	35.5
	C–C sp^3	284.9	23.0
	C–O	285.8	20.3
	C=O	533.5	7.1
	O–C=O	288.7	6.8
N-rGO	C–C sp^2	284.4	69.7
	C–C sp^3	532.7	15.6
	C–O	—	—
	C=O	—	—
	O–C=O	399.1	0.9

Fig. 2 (a) Deconvoluted XPS spectrum of the N1s peak for N-rGO. (b) Graphical representation of the types of nitrogen defects introduced. (c) Deconvoluted N1s peak of g-C_3N_4. (d) Deconvoluted C1s peak of g-C_3N_4. (e) High-resolution XPS spectrum of Re. (f) High-resolution XPS spectrum of Se.

Table 3 Summary of the binding energy of the O1s assignments

Sample	Assignment	Binding energy (eV)
rGO	C–O	532.0
	C=O	533.5
N-rGO	C–O	531.2
	C=O	532.9
$ReSe_2$-rGO	C–O	531.7
	C=O	533.2
$ReSe_2$-N-rGO	C–O	532.2
	C=O	533.5

assigned to the stretching modes of the aromatic C–N heterocycle and the peak at 805 cm^{-1} was assigned to the breathing mode of the triazine units. The peak assigned to the breathing mode of the triazine units was observed to have shifted to 797 cm^{-1} in the heterostructure and the peak was also significantly supressed compared to the pristine g-C_3N_4. This suggests an interaction between the nitrogen groups in the triazine units and the $ReSe_2$ nanostructures as suggested by the XPS analysis.

The TEM images of the rGO, N-rGO, g-C_3N_4 the 2D carbon–$ReSe_2$ heterostructures are shown in Fig. 3.

The TEM image of the $ReSe_2$ nanostructures is shown in Fig. 3(a), the image shows that the $ReSe_2$ nanostructures form in
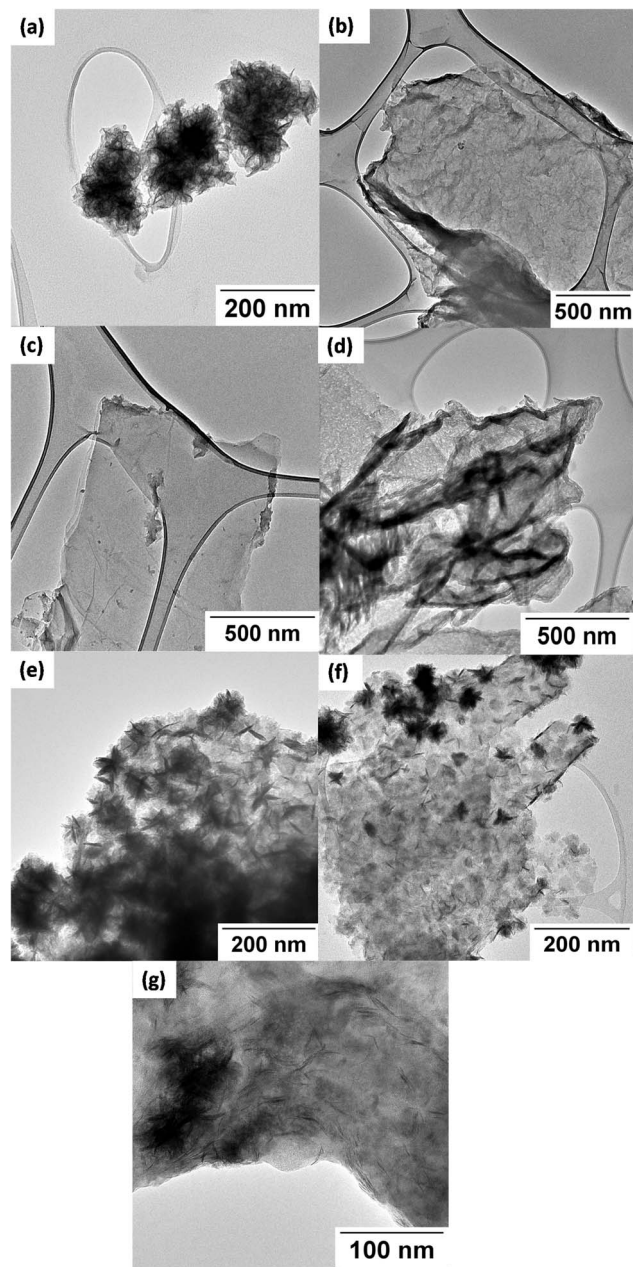
Fig. 3 TEM images of (a) $ReSe_2$ nanoflowers, (b) rGO, (c) N-rGO, (d) g-C_3N_4, (e) $ReSe_2$-rGO, (f) $ReSe_2$-N-rGO, and (g) $ReSe_2$-g-C_3N_4.

a flower-like morphology. The TEM images of rGO and N-rGO are shown in Fig. 3(b) and (c) show that they are both composed of nanosheets that are wrinkled and folded in some regions. The nanosheets are not single sheets, as was already confirmed by the PXRD analysis. There are no significant and notable changes in the morphology of the rGO before and after nitrogen doping as shown in Fig. 3(b) and (c). Fig. 3(d) shows the TEM image of g-C_3N_4, the image shows that the g-C_3N_4 nanosheets that show some degree of folding in some regions, similar to the rGO and N-rGO morphology. The images of $ReSe_2$-rGO and $ReSe_2$-N-rGO are shown in Fig. 3(e) and (f), respectively. The images show that few-layered $ReSe_2$ nanostructures have grown on the surface of the rGO and N-rGO. For the $ReSe_2$-rGO, the $ReSe_2$

nanostructures seem to have completely covered the area of the rGO nanosheets. The same is true for the $ReSe_2$-N-rGO, with some of the areas showing more defined nanoflower structures. The HRTEM image of the $ReSe_2$-g-C_3N_4 in Fig. 3(g) shows that ultrathin $ReSe_2$ nanosheets were able to form on the surface of the g-C_3N_4 nanosheets.

An initial study was conducted to determine the interaction of the Re monomer with the 2D carbon nanostructures, this study was conducted using rGO as the 2D carbon nanostructure of interest. The reaction for the synthesis of $ReSe_2$ was conducted without selenization (introduction of selenium precursor), this was done to specifically determine the interaction of the Re monomer with the rGO nanosheets. The Re monomer – 2D carbon material was then selenized to observe the growth of the $ReSe_2$ nanostructures on the surface of the rGO. A schematic representation of the process before and after selenizations is shown in Fig. 4.

Previous reports have shown that the ReO_4^{2-} anion is formed when NH_2ReO_4 is heated at high temperature.[36] The ReO_4^{2-} is then able to interact with the functional groups on the surface of the rGO, this is in line with what is reported in literature.[36] The TEM image in Fig. 5(a), shows that after the reaction with NH_4ReO_4 the sheet like structure of the rGO does not change. The powder pattern of the rGO-ReO_4^{2-} shows no peaks from anything other than rGO as shown in Fig. S7(a),† this suggests that the NH_4ReO_4 did not convert to any crystalline oxide species such as ReO_3. However, EDS of the rGO-ReO_4^{2-} (Fig. S8†) shows that Re is indeed present which suggests the presence of the ReO_4^{2-} anion. The UV-vis spectrum of the rGO-ReO_4^{2-} (Fig. S7(b)†) shows that characteristic peak for ReO_4^{2-} at 291 nm, which confirms the presence of ReO_4^{2-}.[37] Elemental mapping of rGO-ReO_4^{2-} is shown in Fig. 5(b)–(d). The uniform distribution of the O and Re atoms on the surface of the rGO confirms the interaction of ReO_4^{2-} with the oxygen functional groups on the surface of the rGO.

After selenization (when the selenium precursor in introduced), the formation of the $ReSe_2$ nanostructures can clearly be observed on the surface of the rGO nanostructures. This is shown in Fig. 6(a). An interface can be formed between the $ReSe_2$ nanostructures and the rGO can be clearly observed in Fig. 6(b). A similar phenomenon is observed for the N-rGO 2D carbon nanostructures, after selenization the $ReSe_2$ would grow on the surface of the N-rGO as shown in Fig. 6(c). When g-C_3N_4 was used the type of interaction would involve the ReO_4^{2-} would interact with the nitrogen groups in the triazine ring as alluded to by the XPS and FTIR analysis. After selenization the $ReSe_2$ nanostructures were able to grow on the on the g-C_3N_4 nanostructures as shown in Fig. 6(d). The growth of the $ReSe_2$ nanostructures seems to distort the structure of g-C_3N_4. The well-defined g-C_3N_4 nanosheets seem to form a distorted flocculate-like morphology with $ReSe_2$ nanosheets that have grown on the g-C_3N_4.

Scanning electron microscopy (SEM) was also performed on the heterostructures. Fig. 7(a), (b), and (c) shows the $ReSe_2$-rGO, $ReSe_2$-N-rGO, and $ReSe_2$-g-C_3N_4 heterostructures respectively. The images clearly show that the $ReSe_2$ nanocrystals have grown on the surface of the carbon nanostructures.
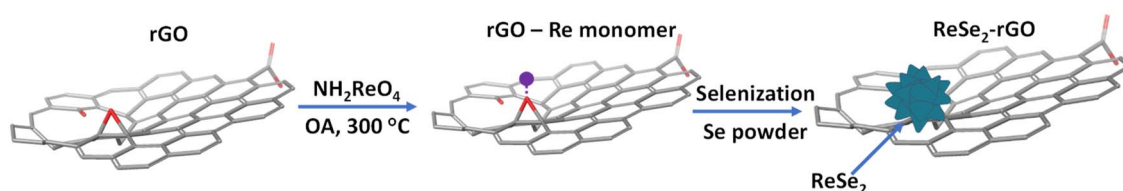
Fig. 4 Schematic representation of the synthesis process for ReSe$_2$-rGO.

The TEM image in Fig. 3(a) already showed that the ReSe$_2$ nanostructures had a pseudo-spherical flower-like morphology. The SEM images show that the flower-like ReSe$_2$ nanostructures have grown on the different 2D carbon nanostructures. The SEM image of the ReSe$_2$-rGO (Fig. 7(a)) shows that the rGO has been completely covered by the ReSe$_2$ nanosheets with agglomeration of the spherical flower-like ReSe$_2$ being observed. This was not the case for the N-rGO (Fig. 7(b)) and g-C$_3$N$_4$ (Fig. 7(c)), there are clearly visible regions where the uncovered N-rGO and g-C$_3$N$_4$ can be observed, this is due to the readily available oxygen containing functional groups on the rGO that ensure maximal formation and growth of the ReSe$_2$ nanostructures on its surface. Energy-dispersive X-ray spectroscopy (EDX) was used to investigate the elemental composition of the heterostructures and the distribution of the ReSe$_2$ nanocrystals on the surface of the 2D carbon nanostructures. The EDX spectra of the heterostructures is shown in Fig. S9 (a), (b), and (c)† for the ReSe$_2$-rGO, ReSe$_2$-N-rGO, and ReSe$_2$-g-C$_3$N$_4$ heterostructures respectively. The spectra show the presence of Re, Se, C, N, Ag, and Pd. Ag and Pd was used to coat the samples to prevent charging. The elemental mapping of the heterostructures is shown in Fig. S10(a)–(c).† The mapping shows that the Se atom distribution overlaps well with the Re mapping, this confirms the formation of ReSe$_2$ nanocrystals on the surface of the 2D carbon nanostructures. The maps also show that the carbon nanostructures are covered by the ReSe$_2$ nanocrystals with some areas of exposed carbon being
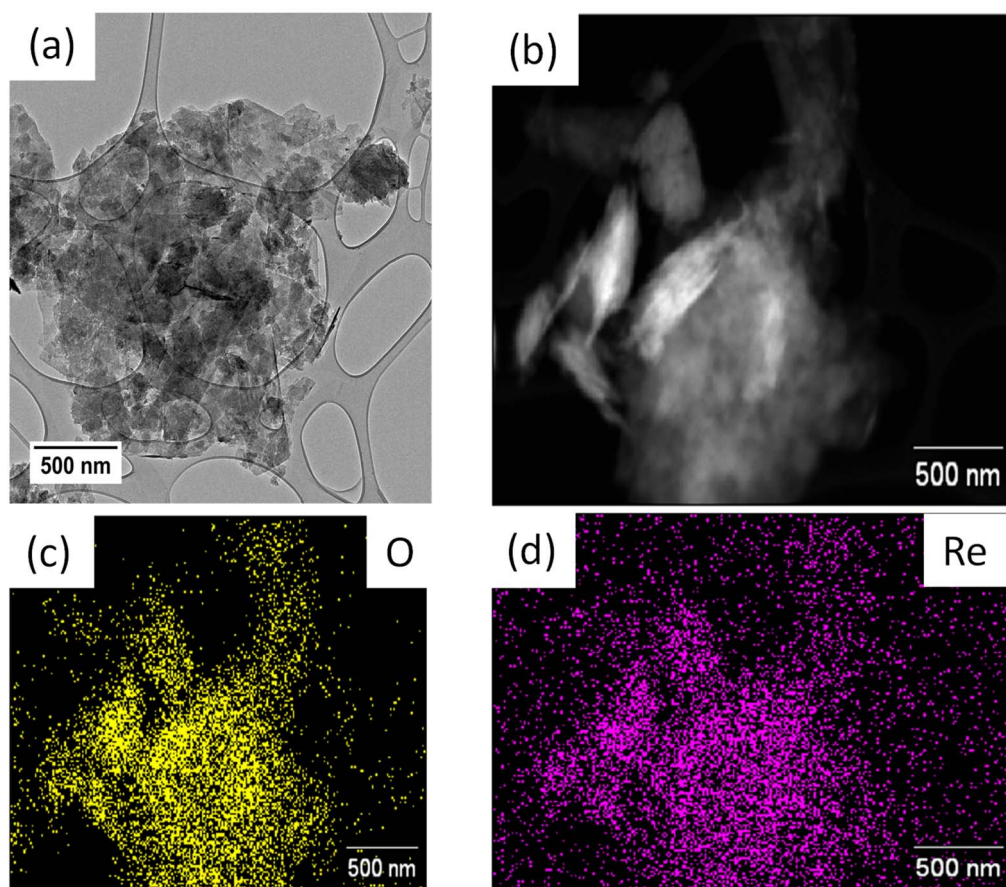

Fig. 5 (a) Sheetlike structure of rGO after introduction of Re monomer. (b) Grey image of rGO-ReO$_4$$^{2-}$. Elemental mapping of (c) oxygen and (d) rhenium.
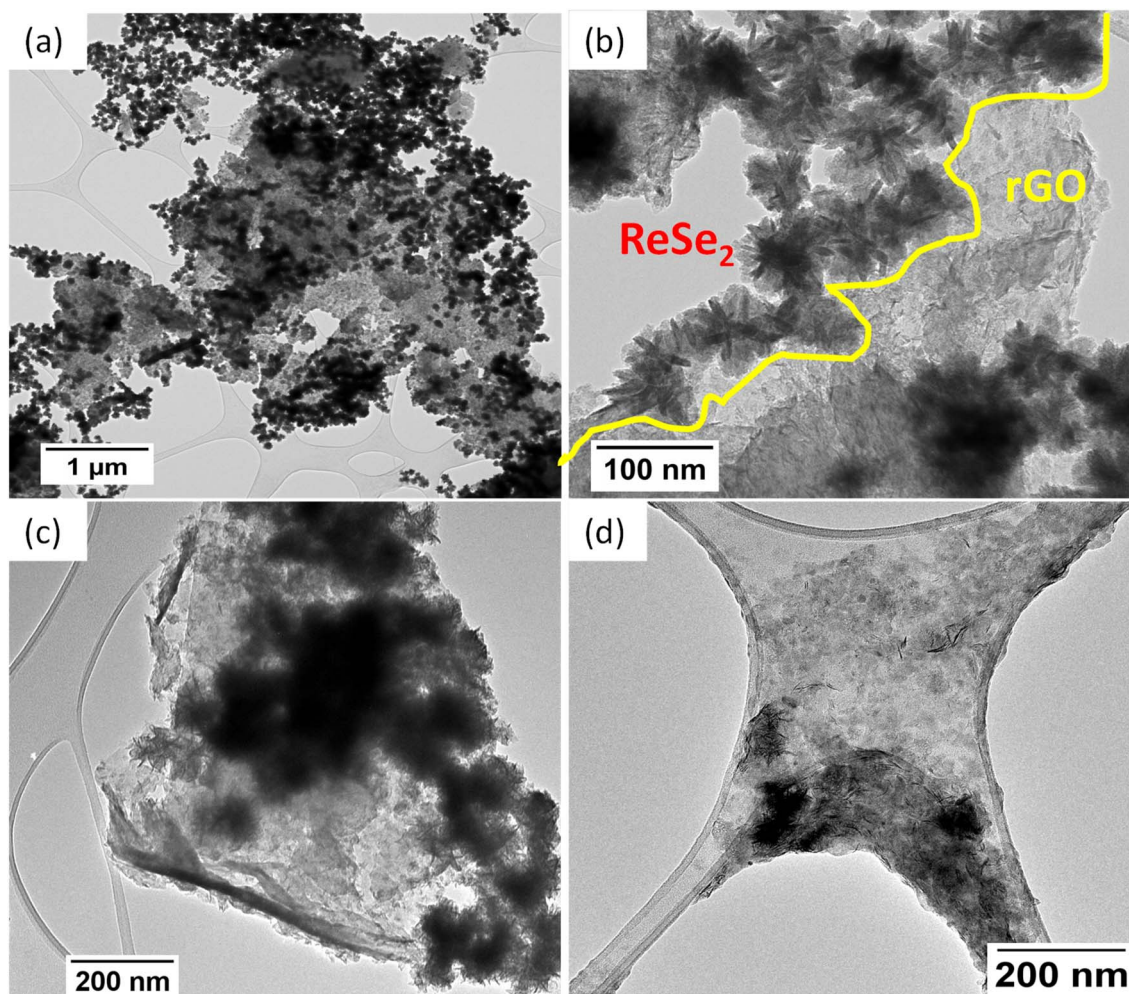
Fig. 6 (a) Formation of the ReSe$_2$-rGO after selenization. (b) Interface between the ReSe$_2$ and the rGO. (c) Formation of ReSe$_2$-N-rGO after selenization. (d) Formation of ReSe$_2$-g-C$_3$N$_4$ after selenization.

observed. The maps also show the presence of oxygen from the surface functional groups.

Thermogravimetric analysis (TGA) was used to investigate the decomposition of the rGO, N-rGO, g-C$_3$N$_4$ and the hetero-structures under an airflow of 20 ml min^{-1}. The decomposition profiles are shown in Fig. 8.

The TGA profiles of the rGO and N-rGO are shown in Fig. 8(a). The initial weight losses on both profiles at ~150 °C are attributed to the evaporation of water molecules adsorbed on the rGO and N-rGO.[38] The second largest mass loss was measured at 6% for rGO and 3% for N-rGO which was attributed to the oxygen-containing functional groups.[39] There is twice the loss of these functional groups in rGO which suggests that the doping process was able to remove functional groups on the surface of the N-rGO beforehand. The largest weight loss between 400–700 °C which accounted for 94% in rGO and 97% in N-rGO was attributed to the decomposition of the carbon skeleton of graphene.[36] The decomposition temperature for this weight loss on N-rGO was slightly higher than that of rGO which was expected as doped carbon structures have been known to be more stable than undoped rGO structures.[40] The difference in

decomposition temperatures can be clearly seen in the derivative decomposition profile in Fig. S11.† The decomposition profile of g-C$_3$N$_4$ is shown in Fig. 8(d), the initial mass loss at ~150 °C was due to the evaporation of water molecules on adsorbed on the g-C$_3$N$_4$. The large mass loss of 96% observed at 520 °C was attributed to the decomposition of the g-C$_3$N$_4$ to carbon and nitrogen containing gases. The TGA curves ReSe$_2$-rGO and ReSe$_2$-N-rGO are shown in Fig. 8(b) and (c), these are shown with the TGA curves of rGO and N-rGO for comparison. The heterostructures show two mass losses, one between 400–500 °C and another between 500 to 600 °C. The first mass loss was measured at 60% for rGO and 63% for N-rGO. The mass loss was attributed to the decomposition of the graphene backbone. The second mass loss was attributed to the decomposition of the oleic acid that is bound to the ReSe$_2$ nanostructures which accounted for 37% and 36% of the ReSe$_2$-rGO and ReSe$_2$-N-rGO respectively. The increase in the temperature of the decomposition compared to literature was attributed to the bound oleic acid (oleic acid interacting with the ReSe$_2$ nanostructures) as opposed to unbound oleic acid.[39] The decomposition profile of ReSe$_2$-g-C$_3$N$_4$ is shown in Fig. 8(d). The
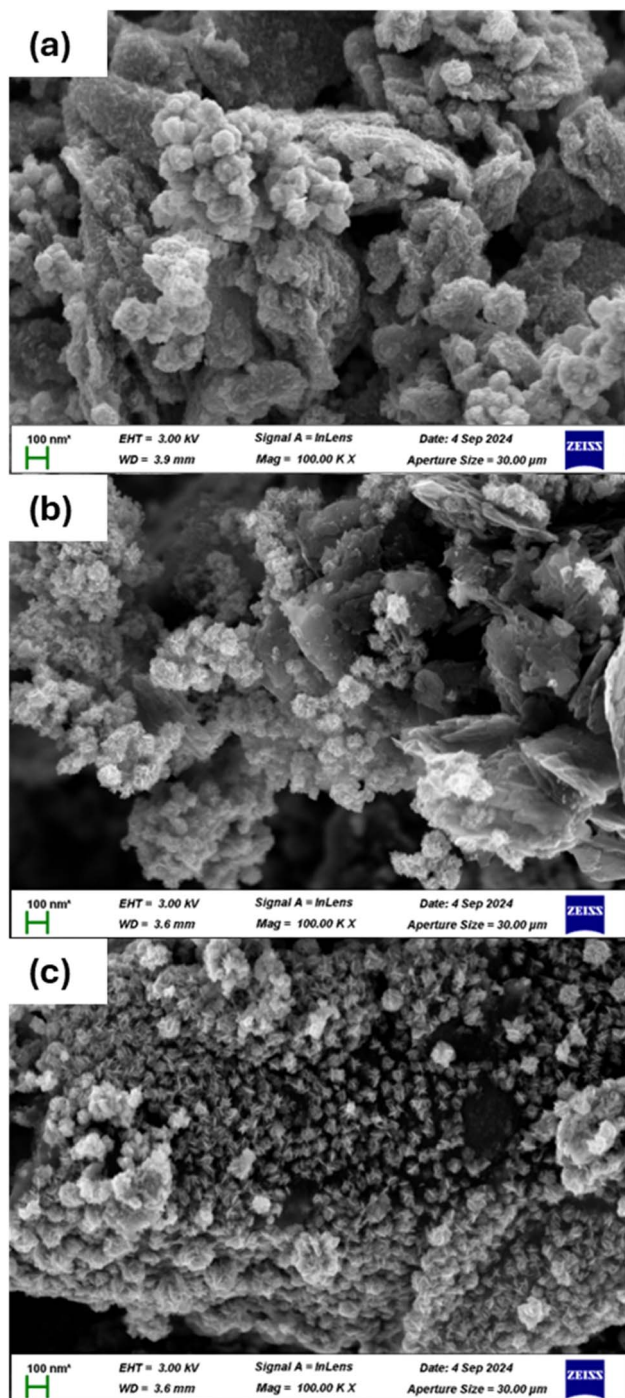
Fig. 7 SEM images of (a) $ReSe_2$-rGO, (b) $ReSe_2$-N-rGO, and (c) $ReSe_2$-g-C_3N_4.

large mass loss accounting to 77% between 400 °C and 600 °C was attributed to the decomposition of g-C_3N_4. The decomposition of the bound oleic acid occurs between 500 °C and 600 °C and accounts for 20% of the mass loss. The final mass loss between 700 °C and 800 °C accounting for ~3% was attributed to the rest of the g-C_3N_4 decomposition. The residues that remained after decomposition accounted for 2.7%, 1.7%, and 0.5% for $ReSe_2$-rGO, $ReSe_2$-N-rGO, and $ReSe_2$-g-C_3N_4

respectively. This suggests that the rGO had a larger catalyst loading of the $ReSe_2$ compared to the N-rGO and g-C_3N_4, this is due to the higher availability of the oxygen containing functional groups on the rGO. The $ReSe_2$-g-C_3N_4 heterostructure had the lowest mass loading of $ReSe_2$, this suggest that the nitrogen defects in the structure of the material may not be as effective at anchoring the $ReSe_2$ compared to the oxygen containing functional groups.

The adsorption–desorption curves of all the nanostructures show a type-IV isotherm with a distinct hysteresis loop (IUPAC classification) as shown in Fig. S12† and 9, this suggests that the nanostructures assume a mesoporous structure.[40]

The BET surface area of the rGO and N-rGO was calculated to be 231.3 m^2 g^{-1} and 236.3 m^2 g^{-1} as shown in Fig. S12(a) and (b).† The surface area of the doped and undoped area is virtually identical which suggests that there was no significant folding or wrinkling of the nanosheets during the doping process which would have reduced the surface area. The surface area of the g-C_3N_4 was measured to be 7.9 m^2 g^{-1}, the surface area is quite low as expected for g-C_3N_4 nanosheets. The BET surface area of the pristine $ReSe_2$ nanoflowers was measured to be 16.6 m^2 g^{-1} as shown in Fig. 9(a). The surface area of the $ReSe_2$-rGO, $ReSe_2$-N-rGO, and $ReSe_2$-g-C_3N_4 was measured to be 36.2 m^2 g^{-1}, 42.2 m^2 g^{-1}, and 26.6 m^2 g^{-1} respectively as shown in Fig. 9(b), (c), and (d). The boosted surface area of the pristine $ReSe_2$ nanoflowers is due to the confined growth of vertically aligned nanosheets on the 2D carbon nanostructures.[41]

Several parameters are used to evaluate the catalytic activity of nanomaterials towards the HER. The polarization curves can be used to determine two useful parameters, which are the onset potential and the overpotential at 10 mA cm^{-2} (η_{10}). The polarisation curves for the pristine $ReSe_2$ and the heterostructures is shown in Fig. 10(a). The onset potential is the lowest potential at which the HER can be produced. A good HER catalyst is characterized by a low onset potential. The onset potential of the pristine $ReSe_2$ nanostructures was determined to be 159 mV. The incorporation of the $ReSe_2$ nanostructures on the carbon nanostructures significantly reduces the onset potential. The onset potential of the $ReSe_2$-rGO, $ReSe_2$-N-rGO, and $ReSe_2$-g-C_3N_4 was measured to be 128 mV, 115 mV, and 135 mV respectively. Forming a heterostructure with the 2D carbon nanostructures seems to improve the catalytic activity. The overpotential at 10 mA cm^{-2} (η_{10}) is a measure of the overpotential at a specified current density, 10 mA cm^{-2} is chosen because it represents the operating current density of a commercial cost-competitive photoelectrochemical cell (PEC). This parameter is useful when comparing the catalytic activity of nanomaterials, an ideal HER catalyst has the lowest possible η_{10}. The η_{10} of the pristine $ReSe_2$ nanostructures was recorded at 331 mV. The η_{10} of the $ReSe_2$ heterostructures were recorded at 259 mV, 218 mV, and 358 mV for the $ReSe_2$-rGO, $ReSe_2$-N-rGO, and $ReSe_2$-g-C_3N_4 respectively. Incorporating the $ReSe_2$ nanostructures on rGO improves the overpotential which is attributed to the improved electron conductivity of the heterostructures. The doping of the rGO with nitrogen further improves the overpotential as expected. This is not the case when g-C_3N_4 was used, which was attributed to the unsuitable
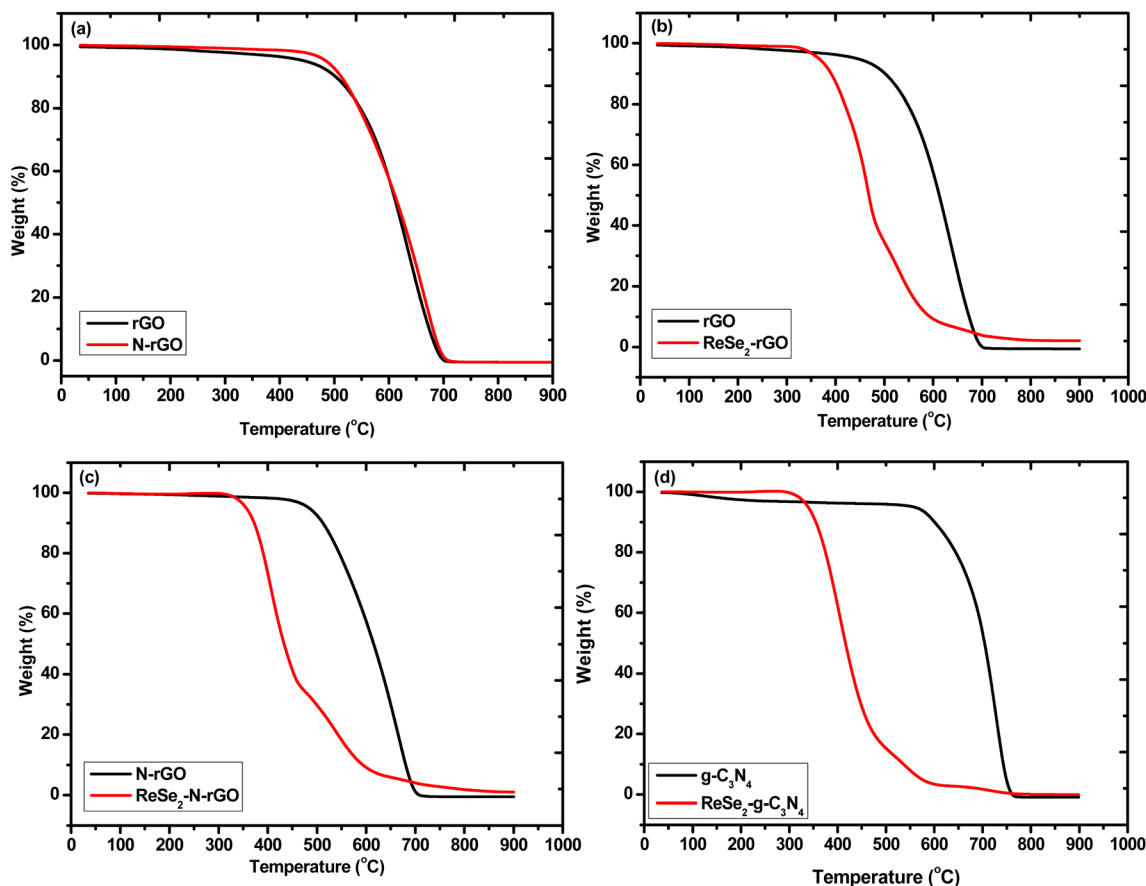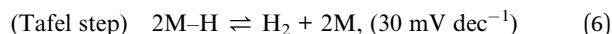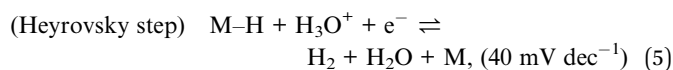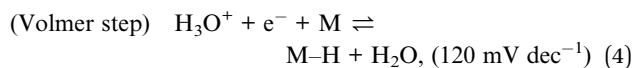
Fig. 8 Decomposition profiles of (a) rGO and N–rGO, (b) rGO and $ReSe_2$–rGO, (c) N–rGO and $ReSe_2$–N–rGO and (d), g-C_3N_4 and $ReSe_2$-g-C_3N_4.

interaction between the $ReSe_2$ and the g-C_3N_4. The Tafel plot analysis is crucial in evaluating the catalytic activity of nanomaterials towards the HER. The Tafel equation ($\eta = b \log J + a$, where η is the overpotential, J is the current density and b is the Tafel slope) fitted to the Tafel plots to determine the Tafel slope.[42] The Tafel slope can be used to gain insights into the mechanistic details of the HER on the specified catalyst. The Tafel slope can be used to determine the rate-limiting step of the reaction and the reaction pathway of the HER on the surface of the nanostructures. The HER in acidic media can be described in three steps:

(Volmer step) $\quad H_3O^+ + e^- + M \rightleftharpoons$
$$M\text{–}H + H_2O, (120 \text{ mV dec}^{-1}) \quad (4)$$

(Heyrovsky step) $\quad M\text{–}H + H_3O^+ + e^- \rightleftharpoons$
$$H_2 + H_2O + M, (40 \text{ mV dec}^{-1}) \quad (5)$$

(Tafel step) $\quad 2M\text{–}H \rightleftharpoons H_2 + 2M, (30 \text{ mV dec}^{-1}) \quad (6)$

The Volmer reaction is the primary discharge step in which protons are adsorbed to active sites on the surface of the catalysts and combine with electrons to form adsorbed hydrogen atoms. This step is followed by either an electrochemical desorption step (Heyrovsky reaction) or a recombination step

(Tafel reaction).[21] The Tafel plots of the pristine $ReSe_2$ and the heterostructure are shown in Fig. 10(b). The Tafel slopes of the $ReSe_2$ nanostructures and the heterostructures were determined to be 97 mV dec^{-1}, 84 mV dec^{-1}, 72 mV dec^{-1}, and 142 mV dec^{-1} for the pristine $ReSe_2$ nanostructures, $ReSe_2$-rGO, $ReSe_2$-N-rGO, $ReSe_2$-g-C_3N_4 respectively. This shows that the HER on the surface of the $ReSe_2$-rGO and $ReSe_2$-N-rGO heterostructures proceeds under the Volmer–Heyrovsky pathway. This pathway involves the adsorption of protons on the surface of the catalyst which then combines with electrons to form adsorbed hydrogen atoms (Volmer step), this is followed by the electrochemical desorption of the hydrogen from the surface of the electrode (Heyrovsky step). The electrochemical desorption is the rate-limiting step in this case. However, the Volmer step is the rate determining step for the HER on the $ReSe_2$-g-C_3N_4 heterostructure. The exchange current density is a useful parameter to probe reaction kinetics, it represents the rate of electron transfer at zero overpotential and is represented in the form of current density. The exchange current density can be determined from the Tafel plot by using the Tafel equation ($\log J_o = a$), where a is the intercept of the Tafel plot. The higher the exchange current density, the better the catalytic performance. The exchange current density was determined to be 0.61 mA cm^{-2}, 0.69 mA cm^{-2}, 0.71 mA cm^{-2}, and 0.38 mA cm^{-2} for $ReSe_2$, $ReSe_2$-rGO, $ReSe_2$-N-rGO, and $ReSe_2$-g-C_3N_4.
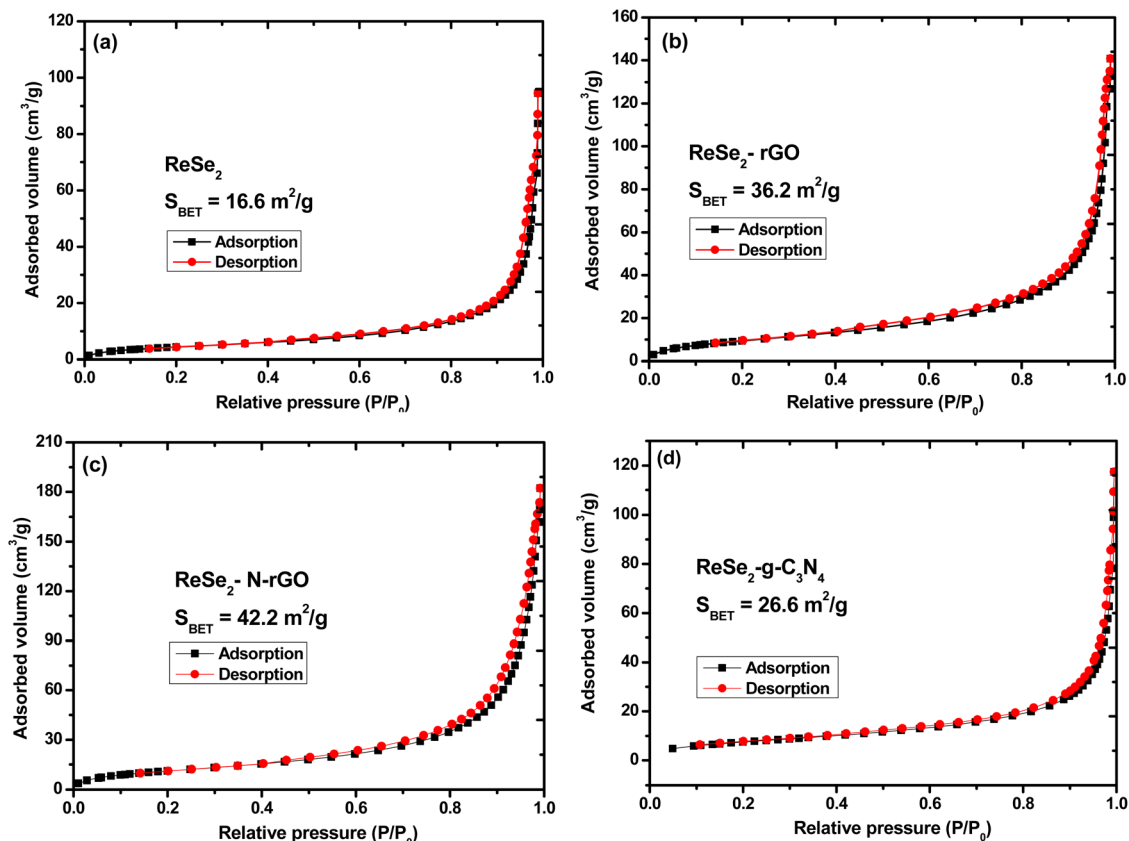
Fig. 9   Adsorption–desorption isotherms of (a) $ReSe_2$, (b) $ReSe_2$-rGO, (c) $ReSe_2$-N-rGO, and (d) $ReSe_2$-g-C_3N_4 .

The exchange current density increases when the $ReSe_2$ nanostructures are grown on rGO and N-rGO. However, the exchange current density decreases when $ReSe_2$ is grown on g-C_3N_4. This is in keeping with what has already been observed with the analysis of the overpotential and the Tafel slope.

The electrochemically active surface area (ECSA) was determined using the C_{dl} (double layer capacitance). The C_{dl} has been shown to be proportional to the ECSA, the C_{dl} was determined using cyclic voltammetry (CV) as shown in Fig. S13.† [37,43] The estimation is done by plotting ΔJ ($J_a - J_c$) vs. the scan rate at 0.41 V vs. RHE which is shown in Fig. 10(c), in this linear plot, the slope is the C_{dl}. The C_{dl} of the nanostructures was determined to be 1.85 mF cm^{-2}, 1.98 mF cm^{-2}, 4.45 mF cm^{-2}, 1.98 mF cm^{-2} for $ReSe_2$, $ReSe_2$-rGO, $ReSe_2$-N-rGO, and $ReSe_2$-g-C_3N_4 respectively. The rGO and N-rGO based heterostructures have a higher ECSA which indicates that the exposure of the active sites was enhanced when the rGO and N-rGO were introduced. The $ReSe_2$-g-C_3N_4 heterostructure had the lowest ECSA, which was expected considering the heterostructure had the lowest loading of the $ReSe_2$ on the surface of g-C_3N_4. The $ReSe_2$ with the nitrogen-doped rGO had a lower ECSA than that of the undoped rGO. This is expected considering the TGA analysis showed that there was much less loading of the $ReSe_2$ catalyst on the nitrogen-doped rGO. However, by every other metric, the $ReSe_2$ catalyst with the nitrogen-doped rGO has better electrocatalytic activity than the $ReSe_2$ with the undoped rGO. This

suggests that the improved catalytic activity of the $ReSe_2$ with the nitrogen-doped rGO is not just due to the improved exposure of the active sites. Since the determination of the ECSA is made using the C_{dl}, the C_{dl} contribution of the 2D carbon nanostructures must also be considered, the C_{dl} contribution of the carbon nanostructures are sure to over inflate the C_{dl} values. There is another approach that can be used to evaluate the $ReSe_2$ catalyst available on the surface of the 2D carbon nanostructures. The irreversible surface oxidation of the $ReSe_2$ nanostructures can be used to investigate ECSA. The anodic peaks shown in Fig. 10(d) represent the surface oxidation process, the area under the peaks represents the amount of charge needed to fully oxidize the surface of the nanostructures.[44] There is significantly more charge required for the oxidation of the $ReSe_2$-rGO, which suggests that there is far more available surface area to oxidize than for the $ReSe_2$-N-rGO and $ReSe_2$-g-C_3N_4. This indicates that the higher catalyst loading on the rGO leads to more available active sites compared to the $ReSe_2$-N-rGO and $ReSe_2$-g-C_3N_4, this is corroborated by the ECSA and TGA. The electrochemical impedance spectroscopy (EIS) was used to study the electron transfer properties of the heterostructures during the HER. The EIS results are represented as Nyquist plots as shown in Fig. 10(e). The equivalence circuit fitted to the data is shown as an insert in Fig. 10(e), the circuit components are shown as R_s (solution resistance), Q_2 (constant phase element), and the R_{ct}
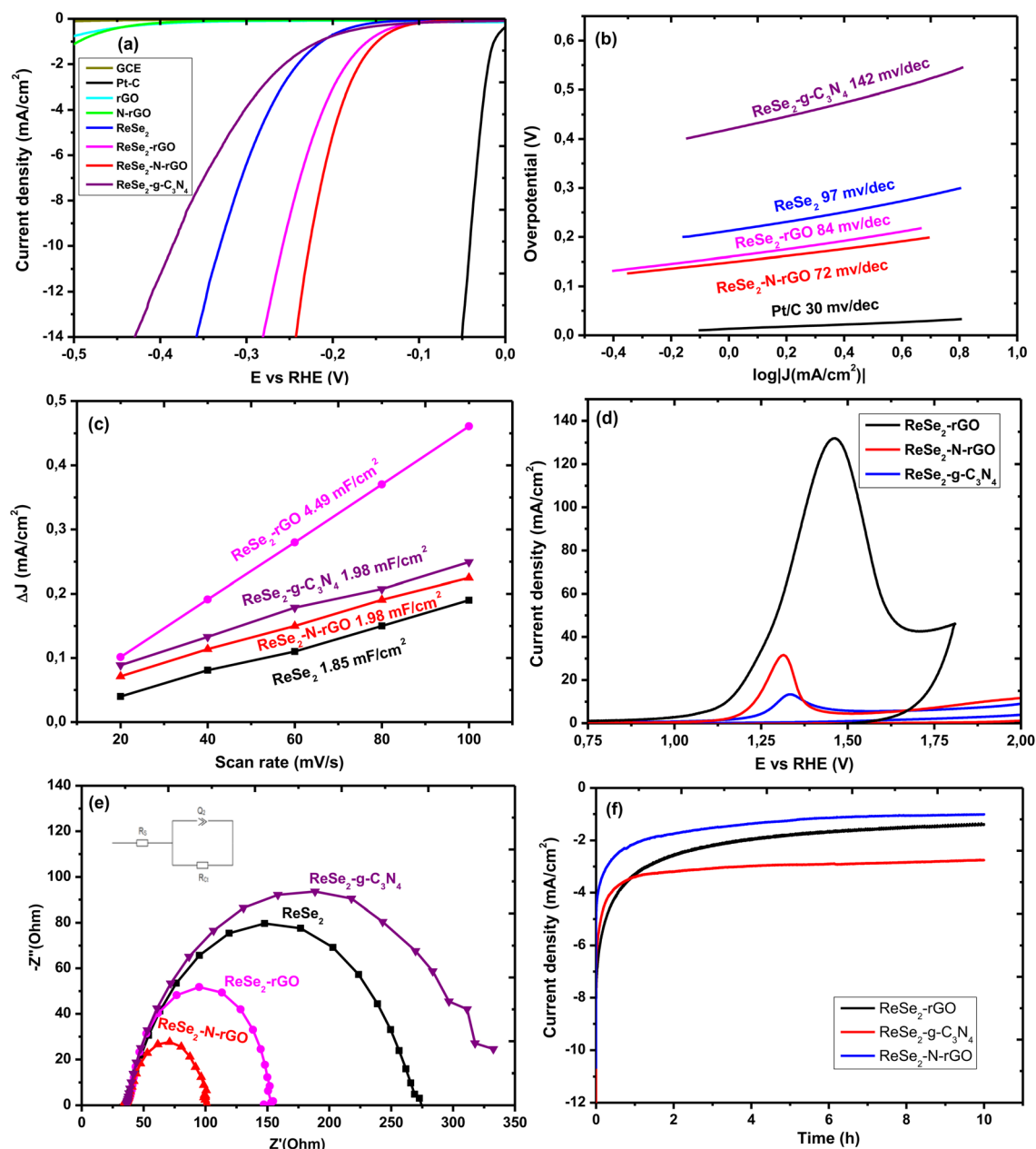
Fig. 10 (a) Polarisation curves of the ReSe₂ nanostructures and their heterostructures. (b) Tafel plots of the ReSe₂ nanostructures and heterostructures. (c) C_{dl} plots of the ReSe₂ nanostructures and heterostructures. (d) Nyquist plots of the ReSe₂ nanostructures and heterostructures. (e) Irreversible surface oxidation profile of ReSe₂-rGO, ReSe₂-N-rGO and ReSe₂-g-C₃N₄. (f) Stability studies of the ReSe₂ nanostructures and heterostructures.

which is the charge transfer resistance. The charge transfer resistance represents the ease or difficulty of charge transfer at the interface between the electrode and the electrolyte. The lower the R_{ct} the better the rate of electron transfer and thus the better the performance of the catalyst. The R_{ct} of the ReSe₂ nanostructures was measured to be 251 Ω. The electron transfer processes improve when the ReSe₂ is incorporated into the doped and undoped rGO. The R_{ct} of the ReSe₂-rGO, ReSe₂-N-rGO, and ReSe₂-g-C₃N₄ was determined to be 117 Ω, 65 Ω and 275 Ω respectively. The electron transfer of the HER processes is more effective in the ReSe₂-N-rGO as compared to the ReSe₂-

rGO. This is due to the improved electron conductivity of the rGO after nitrogen doping. This explains the superior performance of ReSe₂-N-rGO as compared to ReSe₂-rGO even though the ReSe₂-rGO has been shown to have a higher ECSA. This is further confirmed through the computational analysis of the ReSe₂-rGO and ReSe₂-N-rGO. The heterostructures were constructed by attaching the GO sheet and N-rGO to the optimized structure of the ReSe₂ structure. The build structures are shown in Fig. 11. Fig. 11(C) and (F) show the side view of the optimized heterostructure, while Fig. 11(F) shows the top view.
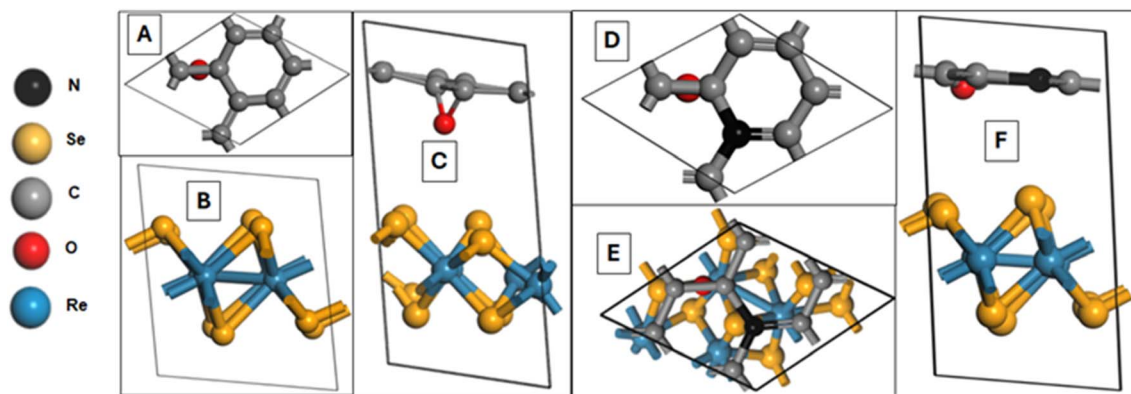
Fig. 11 Optimized geometries of (A) GO sheet, (B) ReSe$_2$ structure, (C) GO/ReSe$_2$ heterostructure, (D) N–rGO sheet, (E) top-view of N–rGO/ReSe$_2$ heterostructure and (F) side-view of N–rGO/ReSe$_2$ heterostructure. The red, black, grey, blue and gold represent the following atoms, oxygen, nitrogen, carbon, rhenium and selenium, respectively.
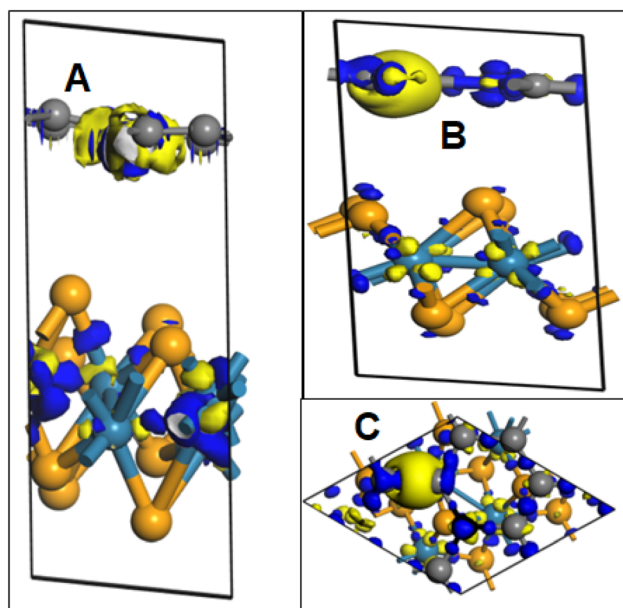

Fig. 12 The three-dimensional (3D) charge density differences of (A) ReSe$_2$-rGO heterostructure, (B) side view of ReSe$_2$-N-rGO heterostructure and (C) top view of ReSe$_2$-N-rGO heterostructure. The yellow and blue colours represent the accumulation and depletion of electrons, respectively.

The charge transfer of the N-rGO and ReSe$_2$ heterostructures were examined using the charge density difference, with an isosurface value of 0.009 e Å^{-3} (Fig. 12).

We contend that there is clear accumulation/depletion of electrons within both heterostructures. The gain of electrons (shown in yellow) and the loss of electrons (shown in blue) from the ReSe$_2$-rGO and ReSe$_2$-N-rGO heterostructures—demonstrates the obvious anisotropic redistribution of electronic charges that occurs upon the formation heterointerfaces (as shown in Fig. 12).[45] ReSe$_2$-rGO heterostructure (Fig. 12(A)), reveals that the more localised 4p state of the Se-atoms and the delocalised Re-atoms in the 6s are the sources of the charge

redistribution. The ReSe$_2$ monolayer shows a very balanced electron accumulation/depletion as electrons are equally distributed within the system. In the upper layer (GO monolayer), the influence of the O-atom shows a high localised charge redistribution of electrons and makes C-atoms delocalised, this is due to the high electronegativity effect of O-atom in the GO/ReSe$_2$ heterostructure system. We observe a high-intensity accumulation of electron charge density within the sphere of O-atom. The oxygen 2p state acts as the charge redistribution localization and the carbon 2p state acts as the charge delocalisation. In the formed π-bonds, oxygen turns to achieve high electron efficiencies as it shows a substantial yellow area.[46]

Fig. 12(B) shows the GO-graphiticN/ReSe$_2$ heterostructure, where we can observe the yellow and blue areas that demonstrate the accumulation/depletion. In the ReSe$_2$ monolayer, the Se-atoms illustrate the depletion of electrons in all sites of the monolayer, this influences Re-atoms that show the high accumulation spheres.[47] As expected in this system, we can observe a high electron charge transportation around the Re-atoms, suggesting that Re-atoms gain electrons through the electron charge reduction of Se-atoms. In the upper layer (GO-graphitic layer), as the N-atom is introduced into the system, we can observe no change in the reduction of high-intensity charge distribution within the O-atom. O-atom shows a very high accumulation of electrons compared to N-atom, this is because oxygen has higher electronegativity than nitrogen. Fig. 12(C) shows the top-view of the GO-graphiticN/ReSe$_2$ heterostructure, although N-atom is gaining electrons as well, oxygen has more accumulation sphere than nitrogen.[47] The accumulation of charge on the O-atom on the surface functional groups observed in the charge difference maps facilitates the transfer of charge (electron transfer) from the ReSe$_2$ to the rGO. The electron transfer is further enhanced by the incorporation on N-doping, this is shown in the accumulation of charge on the N-atom in N-doped rGO. This clearly shows the mechanism by which the N-doping can improve the electron transfer from ReSe$_2$ and N-rGO.[48,49] Coupled with the observed improvement in the R_{ct} of ReSe$_2$-N-rGO, it is evident that the N-doping of the rGO can

RSC Advances

Table 4 Comparison of the catalytic activity of the as synthesized $ReSe_2$, the hybrid nanostructures and their literature counterparts

HER catalyst	Synthesis method	η_{10} (mV)	Tafel slope (mV dec^{-1})	Onset potential (mV)	Ref.
$ReSe_2$@rGO	Hydrothermal	145	40.7	—	36
$ReSe_2$ on carbon cloth	CVD	265	69	—	20
$ReSe_2$ on porous carbon cloth	CVD	200	108	—	50
Treated $ReSe_2$ on porous carbon cloth	CVD	140	64	—	50
$ReSe_2$-rGO	Colloidal	259	84	128	This work
$ReSe_2$-N-rGO	Colloidal	218	72	115	This work
$ReSe_2$-g-C_3N_4	Colloidal	385	142	135	This work

significantly affect the electrocatalytic activity of the heterostructures through the modulation of the electron transfer characteristics of the 2D nanostructures. The $ReSe_2$-g-C_3N_4 heterostructure had the highest R_{ct}, this is due to the weak interaction of the $ReSe_2$ with the nitrogen groups on the g-C_3N_4. The stability of the electrocatalysts was evaluated using chronoamperometry (CA), where the current response of the catalyst after an applied potential is evaluated over time as shown in Fig. 10(f). The $ReSe_2$ and $ReSe_2$-g-C_3N_4 catalysts experience a current drop in the first two hours and then the current begins to stabilize. However, the current response for $ReSe_2$-rGO and $ReSe_2$-N-rGO seems to continue dropping until 4 hours. A comparison of the catalytic activity of the as synthesized $ReSe_2$ heterostructures and their counterparts found in literature that are synthesized with other methods is shown in Table 4. The electrochemical characterisation of the nanostructures compared were conducted in 0.5 M H_2SO_4.

Table 4 The catalytic activity of $ReSe_2$ grown on carbon cloth in other studies is comparable to the catalytic activity of the $ReSe_2$-N-rGO heterostructure. There is currently no work that studies the use of nitrogen doped reduced graphene oxide. The $ReSe_2$@rGO synthesized by Yan *et al.* had higher catalytic activity than the heterostructures synthesized in this work. This was attributed to the catalyst loading; the loading was recorded as 9.5 wt%.[36] This was much higher than the catalyst loading recorded in this work, the catalyst loading was recorded at 2.7% and 1.7% for $ReSe_2$-rGO and $ReSe_2$-N-rGO respectively. This indicates that there is still a lot of work to be done in optimizing the reaction conditions in order to ensure higher catalyst loading. The work by Li *et al.* also showed higher catalytic activity and this was due to heat treatment after the $ReSe_2$ nanostructures on the carbon cloth.[50]

4. Conclusions

In summary, $ReSe_2$ nanostructures were grown on both pristine and nitrogen-doped reduced graphene oxide, and graphitic carbon nitride. Anchored few-layered nanosheets of $ReSe_2$ were shown to grow directly on the rGO, nitrogen-doped rGO, and g-C_3N_4. The few-layered nanosheets tend to overlap and form flower-like $ReSe_2$ nanostructures on the surface of the rGO and N-rGO. However, ultrathin nanosheets of $ReSe_2$ were formed on the g-C_3N_4. TGA and ECSA analysis showed that the undoped rGO was more effective at anchoring the $ReSe_2$ and thus had

nearly double the loading of $ReSe_2$ than the nitrogen-doped rGO. This was attributed to the higher availability of the oxygen functional groups on the surface of the rGO as opposed to the N-rGO. The heptazine and triazine rings of g-C_3N_4 were shown to be poor anchor sites for the $ReSe_2$. The evaluation of the electrocatalytic activity of the heterostructures showed that anchoring the $ReSe_2$ on the carbon nanostructures significantly increases the catalytic activity of the $ReSe_2$ nanostructures. This was true for the $ReSe_2$ grown on both the nitrogen-doped and undoped rGO nanostructures. However, the $ReSe_2$-N-rGO had better catalytic activity toward the HER as opposed to the $ReSe_2$-rGO. This work demonstrated that even though the $ReSe_2$-rGO had a higher loading of $ReSe_2$ which resulted in a higher ECSA, the influence of the superior electron conductivity offered by the nitrogen-doped rGO on the $ReSe_2$-N-rGO resulted in higher catalytic activity towards the HER. It also demonstrates that the type of interaction between the $ReSe_2$ and the carbon nanostructures plays a vital role as the weak interaction between the $ReSe_2$ and g-C_3N_4 results in poor catalytic activity towards the HER.

Data availability

The authors confirm that the data supporting the findings of this study are available within the article and its ESI.† Raw data that supports the findings of this study are available from the corresponding authors, upon reasonable request.

Conflicts of interest

There are no conflicts to declare.

Acknowledgements

References

1 K. Nassiri Nazif, A. Daus, J. Hong, N. Lee, S. Vaziri, A. Kumar, F. Nitta, M. E. Chen, S. Kananian, R. Islam, K. H. Kim,

J. H. Park, A. S. Y. Poon, M. L. Brongersma, E. Pop and K. C. Saraswat, High-Specific-Power Flexible Transition Metal Dichalcogenide Solar Cells, *Nat. Commun.*, 2021, **12**(1), 7034.

2 S. Xu, X. Gao, Y. Hua, A. Neville, Y. Wang and K. Zhang, Rapid Deposition of WS_2 Platelet Thin Films as Additive-Free Anode for Sodium Ion Batteries with Superior Volumetric Capacity, *Energy Storage Mater.*, 2020, **26**, 534–542.

3 N. Rohaizad, C. C. Mayorga-Martinez, Z. Sofer, R. D. Webster and M. Pumera, Niobium-Doped TiS_2: Formation of TiS_3 Nanobelts and Their Effects in Enzymatic Biosensors, *Biosens. Bioelectron.*, 2020, **155**, 112114, DOI: 10.1016/J.BIOS.2020.112114.

4 P. Behera, S. Karunakaran, J. Sahoo, P. Bhatt, S. Rana and M. De, Ligand Exchange on MoS2 Nanosheets: Applications in Array-Based Sensing and Drug Delivery, *ACS Nano*, 2022, **17**(2), 1000–1011.

5 H. Yan, T. Yu, H. Li, Z. Li, H. Tang, H. Hu, H. Yu and S. Yin, Synthesis of Large-Area Monolayer and Few-Layer $MoSe_2$ Continuous Films by Chemical Vapor Deposition without Hydrogen Assistance and Formation Mechanism, *Nanoscale*, 2021, **13**(19), 8922–8930.

6 M. Zhang, Y. Zhu, X. Wang, Q. Feng, S. Qiao, W. Wen, Y. Chen, M. Cui, J. Zhang, C. Cai and L. Xie, Controlled Synthesis of ZrS_2 Monolayer and Few Layers on Hexagonal Boron Nitride, *J. Am. Chem. Soc.*, 2015, **137**(22), 7051–7054.

7 K. S. Novoselov, A. Mishchenko, A. Carvalho and A. H. Castro Neto, 2D Materials and van Der Waals Heterostructures, *Science*, 1979, **2016**(6298), 353.

8 Y. Yan, D. Xiong, B. Tian, L. Zhang, Y. F. Zhu, J. Peng, S. W. Chen, Y. Xiao and S. L. Chou, Expanding the ReS_2 Interlayer Promises High-Performance Potassium-Ion Storage, *ACS Appl. Mater. Interfaces*, 2022, **14**(25), 28873–28881.

9 J. Kibsgaard, Z. Chen, B. N. Reinecke and T. F. Jaramillo, Engineering the Surface Structure of MoS_2 to Preferentially Expose Active Edge Sites for Electrocatalysis, *Nat. Mater.*, 2012, **11**(11), 963–969.

10 Q. Lin, X. Dong, Y. Wang, N. Zheng, Y. Zhao, W. Xu and T. Ding, Molybdenum Disulfide with Enlarged Interlayer Spacing Decorated on Reduced Graphene Oxide for Efficient Electrocatalytic Hydrogen Evolution, *J. Mater. Sci.*, 2020, **55**(15), 6637–6647.

11 K. H. Koh, Y. J. Kim, A. H. B. Mostaghim, S. Siahrostami, T. H. Han and Z. Chen, Elaborating Nitrogen and Oxygen Dopants Configurations within Graphene Electrocatalysts for Two-Electron Oxygen Reduction, *ACS Mater. Lett.*, 2022, **4**(2), 320–328.

12 S. S. Chougule, B. Arumugam, J. K. Alagarasan, I. Hasan, N. Thomas, V. Rajashekar, R. Srinivasan, A. K. Yadav, P. Somu and M. Lee, Amorphous $MoWS_x$ Alloy Nanosheets via Room-Temperature Precipitation Method for Enhanced Electrocatalytic Hydrogen Evolution Reactions, *ACS Appl. Energy Mater.*, 2024, **7**(5), 1949–1960.

13 V. D. Dang, C.-Y. Hsiao, A. Le, V. Q. Le, D. Ho, P. Thao, T.-H. Do and K.-H. Wei, Surface-Plasma-Induced One-Pot Synthesis of N,S-Carbon Dot Intercalated MoS_2/Graphene Nanosheets for Highly Efficient Hydrogen Evolution Reaction, *ACS Appl. Energy Mater.*, 2022, **2022**, 12817–12827.

14 X. Fang, Z. Wang, S. Kang, L. Zhao, Z. Jiang and M. Dong, Hexagonal $CoSe_2$ Nanosheets Stabilized by Nitrogen-Doped Reduced Graphene Oxide for Efficient Hydrogen Evolution Reaction, *Int. J. Hydrogen Energy*, 2020, **45**(3), 1738–1747.

15 H. Li, F. Xie, R. Snyders, C. Bittencourt and W. Li, Structural Engineering of Nitrogen-Doped MoS_2 Anchored on Nitrogen-Doped Carbon Nanotubes towards Enhanced Hydrogen Evolution Reaction, *ChemElectroChem*, 2022, **9**(15), e202200420.

16 K. Nam, H. Chun, J. Hwang, K.-A. Min and B. Han, Pairing of transition metal dichalcogenides and doped graphene for catalytically dual active interfaces for the hydrogen evolution reaction, *ACS Sustain. Chem. Eng.*, 2020, **8**(29), 10852–10858.

17 Y. Sun, V. Kumar and K. H. Kim, The Assessment of Graphitic Carbon Nitride (g-C_3N_4) Materials for Hydrogen Evolution Reaction: Effect of Metallic and Non-Metallic Modifications, *Sep. Purif. Technol.*, 2023, **305**, 122413.

18 E. J. Lin, Y. B. Huang, P. K. Chen, J. W. Chang, S. Y. Chang, W. T. Ou, C. C. Lin, Y. H. Wu, J. L. Chen, C. W. Pao, C. J. Su, C. H. Wang, U. S. Jeng and Y. H. Lai, Graphitic Carbon Nitride Embedded with Single-Atom Pt for Photo-Enhanced Electrocatalytic Hydrogen Evolution Reaction, *Appl. Surf. Sci.*, 2023, **615**, 156372.

19 M. Cao, X. Zhang, J. Qin and R. Liu, Enhancement of Hydrogen Evolution Reaction Performance of Graphitic Carbon Nitride with Incorporated Nickel Boride, *ACS Sustain. Chem. Eng.*, 2018, **6**(12), 16198–16204.

20 J. Li, Q. Zhou, C. Yuan, P. Cheng, X. Hu, W. Huang, X. Gao, X. Wang, M. Jin, R. Nötzel, G. Zhou, Z. Zhang and J. Liu, Direct Growth of Vertically Aligned $ReSe_2$ Nanosheets on Conductive Electrode for Electro-Catalytic Hydrogen Production, *J. Colloid Interface Sci.*, 2019, **553**, 699–704.

21 Z. B. Ndala, S. S. Nkabinde, N. P. Shumbula, O. A. Makgae, T. Kolokoto, M. Ek, S. S. Gqoba, C. E. Linganiso, P. S. Mdluli and N. Moloto, Unraveling the Effects of Surface Functionalization on the Catalytic Activity of ReSe2 Nanostructures towards the Hydrogen Evolution Reaction, *Appl. Surf. Sci.*, 2023, **612**, 155971.

22 A. Verma, S. M Rangappa, S. Ogata and S. Siengchin, *Forcefields for Atomistic-Scale Simulations: Materials and Applications*, 2022, vol. 99.

23 J. P. Perdew and K. Burke, Generalized Gradient Approximation for the Exchange-Correlation Hole of a Many-Electron System, *Phys. Rev. B:Condens. Matter Mater. Phys.*, 1996, **54**(23), 16533.

24 J. P. Perdew, K. Burke and M. Ernzerhof, Generalized Gradient Approximation Made Simple, *Phys. Rev. Lett.*, 1996, **77**(18), 3865.

25 P. Das, Q. Fu, X. Bao and Z. S. Wu, Recent Advances in the Preparation, Characterization, and Applications of Two-Dimensional Heterostructures for Energy Storage and Conversion, *J. Mater. Chem. A*, 2018, **6**(44), 21747–21784.

26 Y. Kauffmann, S. H. Oh, C. T. Koch, A. Hashibon, C. Scheu, M. Rühle and W. D. Kaplan, Quantitative Analysis of Layering and In-Plane Structural Ordering at an Alumina–Aluminum Solid–Liquid Interface, *Acta Mater.*, 2011, **59**(11), 4378–4386.

27 P. Kumar Singh, Impact of high temperature thermal reduction on microstructure, crystallinity and surface topography of reduced graphene oxide, *Mater. Today: Proc.*, 2023, DOI: 10.1016/j.matpr.2023.02.169.

28 X. Mu, B. Yuan, X. Feng, S. Qiu, L. Song and Y. Hu, The Effect of Doped Heteroatoms (Nitrogen, Boron, Phosphorus) on Inhibition Thermal Oxidation of Reduced Graphene Oxide, *RSC Adv.*, 2016, **6**(107), 105021–105029.

29 L. Lin, H. Ou, Y. Zhang and X. Wang, Tri-s-triazine-Based Crystalline Graphitic Carbon Nitrides for Highly Efficient Hydrogen Evolution Photocatalysis, *ACS Catal.*, 2016, **6**(6), 3921–3931.

30 L. Wei, P. Wang, Y. Yang, R. Luo, J. Li, X. Gu, Z. Zhan, Y. Dong, W. Song and R. Fan, Facile Synthesis of Nitrogen-Doped Reduced Graphene Oxide as an Efficient Counter Electrode for Dye-Sensitized Solar Cells, *J. Nanopart. Res.*, 2018, **20**(4), 1–12.

31 G. Witjaksono, M. Junaid, M. H. Khir, Z. Ullah, N. Tans, M. S. B. M. Saheed, M. A. Siddiqui, S. S. Ba-Hashwan, A. S. Algamili, S. A. Magsi, M. Z. Aslam and R. Nawaz, Effect of Nitrogen Doping on the Optical Bandgap and Electrical Conductivity of Nitrogen-Doped Reduced Graphene Oxide, *Molecules*, 2021, **26**(21), 6424.

32 Z. Xing, Z. Ju, Y. Zhao, J. Wan, Y. Zhu, Y. Qiang and Y. Qian, One-Pot Hydrothermal Synthesis of Nitrogen-Doped Graphene as High-Performance Anode Materials for Lithium Ion Batteries, *Sci. Rep.*, 2016, **6**(1), 1–10.

33 Y. Tian, Y. Y. Cao, F. Pang, G. Q. Chen and X. Zhang, Ag Nanoparticles Supported on N-Doped Graphene Hybrids for Catalytic Reduction of 4-Nitrophenol, *RSC Adv.*, 2014, **4**(81), 43204–43211.

34 S. Lu, L. Sui, M. Wu, S. Zhu, X. Yong, B. Yang, S. Lu, S. Zhu, B. Yang, X. Yong, L. Sui and M. Wu, Graphitic Nitrogen and High-Crystalline Triggered Strong Photoluminescence and Room-Temperature Ferromagnetism in Carbonized Polymer Dots, *Adv. Sci.*, 2019, **6**(2), 1801192.

35 S. Guo, Z. Deng, M. Li, B. Jiang, C. Tian, Q. Pan and H. Fu, Phosphorus-Doped Carbon Nitride Tubes with a Layered Micro-Nanostructure for Enhanced Visible-Light Photocatalytic Hydrogen Evolution, *Angew. Chem., Int. Ed.*, 2016, **55**(5), 1830–1834.

36 Y. Yan, S. Xu, H. Li, N. C. S. Selvam, J. Y. Lee, H. Lee and P. J. Yoo, Perpendicularly Anchored ReSe₂ Nanoflakes on Reduced Graphene Oxide Support for Highly Efficient Hydrogen Evolution Reactions, *Chem. Eng. J.*, 2021, **405**, 126728.

37 J. Louis-Jean, H. Jang, K. V. Lawler, P. M. Forster, J. Ash and F. Poineau, Preparation and Characterization of Benzotriazolium Perrhenate, *Inorg. Chim. Acta*, 2019, **498**, 119121.

38 L. Huang, P. Zhu, G. Li, D. Lu, R. Sun and C. Wong, Core–Shell SiO₂@RGO Hybrids for Epoxy Composites with Low Percolation Threshold and Enhanced Thermo-Mechanical Properties, *J. Mater. Chem. A*, 2014, **2**(43), 18246–18255.

39 A. Kukreja, B. Kang, S. Han, M. K. Shin, H. Y. Son, Y. Choi, E. K. Lim, Y. M. Huh and S. Haam, Inner Structure- and Surface-Controlled Hollow MnO Nanocubes for High Sensitive MR Imaging Contrast Effect, *Nano Convergence*, 2020, **7**(1), 1–11.

40 C. Tian, J. Wu, Z. Ma, B. Li, P. Li, X. Zu and X. Xiang, Design and Facile Synthesis of Defect-Rich C-MoS₂/RGO Nanosheets for Enhanced Lithium–Sulfur Battery Performance, *Beilstein J. Nanotechnol.*, 2019, **10**, 2251–2260.

41 M. M. Baig, E. Pervaiz, M. Yang and I. H. Gul, High-Performance Supercapacitor Electrode Obtained by Directly Bonding 2D Materials: Hierarchal MoS₂ on Reduced Graphene Oxide, *Front. Mater.*, 2020, **7**, 580424.

42 Q. Huang, B. Xia, M. Li, H. Guan, M. Antonietti and S. Chen, Single-zinc vacancy unlocks high-rate H₂O₂ electrosynthesis from mixed dioxygen beyond Le Chatelier principle, *Nat. Commun.*, 2024, **15**(1), 1–10.

43 F. Qi, X. Wang, B. Zheng, Y. Chen, B. Yu, J. Zhou, J. He, P. Li, W. Zhang and Y. Li, Self-Assembled Chrysanthemum-like Microspheres Constructed by Few-Layer ReSe₂ Nanosheets as a Highly Efficient and Stable Electrocatalyst for Hydrogen Evolution Reaction, *Electrochim. Acta*, 2017, **224**, 593–599.

44 J. D. Benck, T. R. Hellstern, J. Kibsgaard, P. Chakthranont and T. F. Jaramillo, Catalyzing the Hydrogen Evolution Reaction (HER) with Molybdenum Sulfide Nanomaterials, *ACS Catal.*, 2014, **4**(11), 3957–3971.

45 T. L. Tansley, Chapter 6 Heterojunction Properties, *Semicond. Semimetals*, 1971, **7**, 293–368.

46 N. H. Lam, J. H. Ko, B. K. Choi, T. T. Ly, G. Lee, K. Jang, Y. J. Chang, A. Soon and J. Kim, Direct Characterization of Intrinsic Defects in Monolayer ReSe₂ on Graphene, *Nanoscale Adv.*, 2023, **5**(20), 5513–5519.

47 J. A. A. Mehrez, Y. Zhang, M. Zeng, J. Yang, N. Hu, T. Wang, L. Xu, B. Li, Y. González-Alfaro and Z. Yang, Nitrogen-Based Gas Molecule Adsorption on a ReSe₂ Monolayer via Single-Atom Doping: A First-Principles Study, *Langmuir*, 2024, **40**(15), 7843–7859.

48 Y. Wang, F. Lu, K. Su, N. Zhang, Y. Zhang, M. Wang and X. Wang, Engineering Mo-O-C Interface in MoS₂@rGO via Charge Transfer Boosts Hydrogen Evolution, *Chem. Eng. J.*, 2020, **399**, 126018.

49 X. Xu, W. Xu, L. Zhang, G. Liu, X. Wang, W. Zhong and Y. Du, Interface Engineering Heterostructured MoS₂/WS₂-Reduced Graphene Oxide for Enhanced Hydrogen Evolution Electrocatalysts, *Sep. Purif. Technol.*, 2021, **278**, 119569.

50 J. Li, Y. Liu, C. Liu, W. Huang, Y. Zhang, M. Wang, Z. Hou, X. Wang, M. Jin, G. Zhou, X. Gao, Z. Zhang and J. Liu, Enhanced charge transport in ReSe₂-based 2D/3D electrodes for efficient hydrogen evolution reaction, *Chem. Commun.*, 2020, **56**(2), 305–308.